Metal Phthalocyanines Encapsulated in Faujasite Zeolites for Gas-Phase CO Oxidation

Ethan P. Iaia,[1] Ganesh R. Rana,[2] Ademola Soyemi,[1] Ambar B. Shrestha,[2] Mary Elizabeth S. Martin,[1] Jenna L. Groeber,[1] Charles R. Diemer,[1] Tibor Szilvási,[1] Martin G. Bakker,[2] James W. Harris[1*]

1. Department of Chemical and Biological Engineering, The University of Alabama, Tuscaloosa, AL, 35487
2. Department of Chemistry & Biochemistry, The University of Alabama, Tuscaloosa, AL, 35487

Abstract

Existing metal-containing porous catalysts have inherent heterogeneity in metal species, rendering it difficult to compare reactivity across varied catalyst formulations without first developing active site quantification protocols. The supercages of faujasite zeolites (FAU) are large enough to confine metal phthalocyanines (MPCs), together serving as a well-defined active center for experimental and computational catalyst characterization. Deviations in zeolite synthesis conditions from prior literature were required to obtain phase-pure FAU.Metal perchloro-, perfluoro-, and perhydrogenated phthalocyanines ($MPCCl_{16}$, $MPCF_{16}$, and MPC; M=Cr, Mn, Fe, Co, Ni, Cu, Zn), were encapsulated into FAU zeolites via hydrothermal synthesis (MPC@FAU) and deposited onto the external surfaces by post-synthetic deposition (MPC/FAU). These MPC@FAU catalysts were tested as catalysts for CO oxidation with dioxygen at 298 K and their reactivity compared to that of silica-supported PdAu nanoparticles and cobalt-nitrogen-doped carbon (Co-N-C). Initial CO_2 site time yields were greater than the analogous metal-ion-exchanged zeolites (by ~50×). However, this initial activity decreased with time on stream for all MPC samples tested, and the cause of this deactivation is explored herein. Stable CO_2 formation rates with time on stream observed over $PdAu/SiO_2$ and Co-N-C suggest that deactivation observed over MPC@FAU samples is distinct and not an artifact of the experimental apparatus. Density functional theory calculations suggest an O_2-activation mechanism, aided by the co-adsorption of CO on the pyrrole N of the MPC and an axial ligand that can provide additional electron density to reduce the barrier for O_2 bond breaking, consistent with observed catalytic activity at room temperature and that MPCs feature a distinct reaction mechanism from metal-N-doped carbon structural analogs. Nevertheless, the reactivity of MPC@FAU catalysts for gas-phase CO oxidation with dioxygen at ambient temperature indicates that they may share similar functionality to metal-nitrogen doped carbons and have the potential to serve as model catalysts for gas-phase chemistries.

*Corresponding author: james.harris@eng.ua.edu

Keywords: molecular complexes, zeolites, oxidation, deactivation, carbon monoxide, mechanism

1. Introduction

Synthetic analogs of metalloenzymes are of interest in alkane partial oxidation to alcohols, as they may limit overoxidation and improve selectivity to desired products.[1] Many previous works have focused on zeolites and metal organic frameworks (MOFs), which are comprised of microporous voids of varied connectivities, which can be fine-tuned to simulate the structure and reactivity of metalloenzymes.[2] However, the local and secondary structures of extra framework metal sites supported upon these materials are often non-uniform. Zeolites contain positively charged cations, usually H^+, Na^+ or NH_4^+, that can be exchanged for metallic cations. Not all ion-exchange sites are identical within the zeolite framework, depending on the number of crystallographically unique tetrahedral sites ("T-sites") and the local distributions of framework aluminum atoms and silanol groups.[3, 4] Additionally, it can be difficult to completely exchange one ion for another, leading to a distribution of exchanged cations.[5, 6] Metal sites within MOFs can be difficult to access as the metal sites can become coordinately saturated with framework ligands.[7] Increased uniformity in metal active sites would simplify characterization and the development of structure-function relationships for these catalytic systems.

Square planar iron-containing molecular complexes, such as iron porphyrin and phthalocyanine, are known catalysts for liquid-phase oxidation of alkanes,[8] olefins,[9] and aromatics[10, 11] with peroxide-based oxidants, and have been shown to be stable with repeated use.[12, 13] The metal binding site in phthalocyanine has a four-coordinate planar structure with nitrogen ligands ($M\text{-}N_4$), analogous to the most reactive sites in metal nitrogen-doped carbons (M-N-Cs) for the oxygen reduction reaction (M=Fe, Co, Cr, Mn).[14, 15] These M-N-Cs have shown comparable activity to Pt/C catalysts in the oxygen reduction reaction,[16, 17] leading to their application in thermal catalysis, such as the oxidative dehydrogenation of alcohols and the dehydrogenation of

alkanes.[18] Co-N-C has recently been applied to the low-temperature aerobic oxidation of carbon monoxide.[19] Iron phthalocyanine (FePC) contains square planar iron sites similar to those found in cytochrome P-450 metalloenzymes,[1, 20] Fe ion exchanged zeolites, and Fe-MOFs that catalyze liquid-phase alkane oxidation reactions.[21] FePC can be encapsulated within faujasite (FAU) zeolite, as the diameter of phthalocyanine is similar to that of FAU supercage (~1.2 nm). Encapsulation of a molecular complex like phthalocyanine can lead to formation of uniform active sites and avoid the structural heterogeneity of Fe-MOFs,[2] iron ion-exchanged zeolites,[22] and zeolite-encapsulated metal cations.[23] This results in a catalyst with square planar metal centers that are unsaturated and protected by the zeolite structure, reminiscent of the structure and functionality of cytochrome P-450.[20]

The performance of metal phthalocyanines (MPCs) for catalysis in solution can be limited by their low solubility (~0.0026 g cm^{-3} for $CuPCCl_{16}$ in a pH 12.8 solution).[24] Furthermore, metal phthalocyanines can form aggregates in solution, which are typically less reactive.[25] When phthalocyanines are used for gas-phase catalysis, the solubility of the complex is irrelevant. Furthermore, encapsulation of MPCs within FAU supercages provides site isolation (given the similar size of the encapsulating void and the encapsulated macrocycle), avoiding deleterious dimerization.[26]

There is little previous work involving gas-phase reactions over MPCs. FePC was found to decompose nitric oxide in the gas-phase, resulting in a strongly adsorbed oxygen on the iron.[27] FePC encapsulated in FAU, as well as other MPCs, were reported for oxidation of methane, however, little data was given to ensure that the observed combustion products were not the result of combustion of the MPCs.[28] Romanovsky and Gabrielov[29] reported CO oxidation with O_2, and NO reduction with CO and H_2, over a range of MPCs encapsulated in FAU via reaction of ion-

exchanged metal carbonyls in FAU with dichlorobenzene to form MPCs ("ship-in-a-bottle" syntheses). Rates of CO oxidation were measured by pressure drop, with measurable reactivity even at 195 K.[29] Cumulative turnover numbers (TONs) were ~1000x higher over CoPC@FAU than Co/FAU, and three times higher over CoPC@FAU than CoPC,[29] though the reaction temperature for these data was not reported. NO conversions during NO reduction by H_2 (548 K) over CoPC@FAU, FePC@FAU, NiPC@FAU were 100%, 68%, and 22%, respectively, while RuPC@FAU and OsPC@FAU were inactive.[29] Similar trends were observed for NO reduction with CO (548 K).[29] During N_2O reduction by CO, FePC@FAU was reported to give the highest N_2O conversion (19%), while the other MPC@FAU samples all had similar N_2O conversions (4-9%).[29] These results suggest that MPC@FAU catalysts can perform gas-phase reactions, and that differences in reactivity may be observed with the identity of the metal central atom. Furthermore, use of "ship-in-a-bottle" syntheses has the potential to result in a distribution of sites, including ion exchanged sites that are not (fully) converted to MPCs.[30]

Here, we report a "bottom-up" hydrothermal synthesis protocol for a series of MPC@FAU catalyst samples, including physicochemical and spectroscopic characterization of their structure and adsorptive properties that demonstrate minimal phase impurities or amorphous material. We report trends in reactivity as a function of metal binding site identity (i.e., Cr, Mn, Fe, Co, Ni, Cu, Zn) and peripheral substituents of the MPCs (i.e., H, F, Cl, $(SO_3)_2$) for CO oxidation with O_2. These results are supported by calculations by DFT. We have performed electronic structure calculations to give insight into the geometry of FAU-encapsulated MPCs, binding energies of CO and O_2 on the MPCs, possible reaction mechanism, the UV-Vis, and X-ray adsorption (XAS) spectra of the series of MPCs studied in this work. Together, these findings show that metal

phthalocyanine complexes encapsulated in faujasite zeolites are active in gas-phase CO oxidation and show promise as a useful model catalyst for further catalytic studies.[30]

2. Experimental methods

2.1 Catalyst Naming Scheme

For the remainder of the manuscript, catalysts will be defined as $MPCX_{16}$+Z, where M is the identity of the central metal atom (see Figure S.1), X is the identity of the peripheral substituents (phthalocyanine has 16 peripheral substituent positions, if X is less than 16, the remaining substituents are H), and Z is the zeolite topology. The "+" will be replaced by either and "@" which denotes that the complex is encapsulated in the zeolite, or "/" which denotes that the complex is deposited on surface. M/FAU denotes an ion-exchanged sample. See Section S.1 for more details.

2.2 Catalyst synthesis

2.2.1 Synthesis of $FePCF_{16}$ and $CoPCF_{16}$

$FePCF_{16}$ and $CoPCF_{16}$ was synthesized according to previous work,[26] with a slightly different purification method. First, 2.44 g (14 mmol) of iron or cobalt acetate (Acros Organics, 95%) and 14 g (70 mmol) of 3,4,5,6-tetrafluoro phthalonitrile (AmBeed, 97%) were transferred into an oven-dried 250 cm^3 round bottom flask (RBF) containing a magnetic stir bar. Next, 40 cm^3 of 1-methyl naphthalene (City Chemical LLC, 99%) was added to the flask as solvent. The mixture was heated to reflux (523 K) and held for 24 h. After 24 h, the content was cooled to ambient temperature and filtered by vacuum filtration. A dark blueish green residue/filter cake was obtained. These solids were crushed into a powder and washed with water, benzene (Millipore, 99%), acetone (Alfa Aesar, 99.5%), diethyl ether (Avantor, 99%), and then hexane (VWR, 99%; 40-50 cm^3 of each solvent per gram solid). Then the product was left to dry under rough vacuum (~0.1kPa) at ambient

temperature. % Yield, 41.7%, 5.0 g, 5.83 mmol. UV-Vis (acetone) λ_{max} (log ε): 623 (4.47), MALDI-TOF (reflector positive mode, CCA matrix and red-P as calibrant): m/z, 855.895 $[FeC_{32}F_{16}N_8]+$.

2.2.2 Synthesis of Na/FAU and MPC@FAU

Faujasite zeolite catalysts were synthesized according to a procedure modified from previous literature.[24] The procedure was modified to use aluminum hydroxide instead of aluminum isopropoxide due to phase impurities in final product.[31] First, seven grams of LUDOX HS-30 (Sigma Aldrich, 30 wt%), 0.699 g of aluminum hydroxide (Sigma Aldrich, 51 wt% Al_2O_3), 2.31 g of sodium hydroxide (Sigma Aldrich, 97%), and 21.14 g of Millipore water (18.2 MΩ) were added to a 60 cm^3 perfluoroalkoxy alkane (PFA) jar (Savillex) along with a stir bar (30 mm, VWR). As synthesized FAU zeolite samples with no MPC will be denoted as "Na/FAU". For MPC@FAU samples, 0.075 g of the respective phthalocyanine were added to this mixture. MPCs used include $CuPCCl_{16}$ (Sigma Aldrich, 100%), $CrPCCl_{16}$ (Porphychem, >95%), $FePCCl_{16}$ (Porphychem, >95%), $MnPCCl_{16}$ (Porphychem, >95%), $NiPCCl_{16}$ (Porphychem, >95%), $ZnPCCl_{16}$ (Porphychem, >95%), $ZnPCF_{16}$ (Sigma Aldrich, 90%),The mixture was stirred while capped at ambient temperature for 24 h, then placed in a polytetrafluoroethylene (PTFE)-lined 45 cm^3 acid digestion vessel (Parr Instrument Co.). The vessel was then placed in an oven at 358 K for 36 h. The sample was then removed and washed five times with water (~50 g water per g sample) via vortex mixing (VWR) followed by centrifugation (Beckman Coulter Allegra X-30R, 133 Hz for 360 s, 50 cm^3 centrifuge tubes) and dried overnight in a gravimetric oven held at 363 K to obtain the as-prepared, "unwashed" sample. Samples were then washed by either further vortex mixing and centrifugation or Soxhlet extraction (*vide infra*).

2.2.3 Synthesis of M/FAU

To ion-exchange FAU, 0.3 g of uncalcined Na/FAU and 100 cm^3 of 0.0003 M solution of the desired metal nitrate salt in millipore water were added to a 250 cm^3 PFA jar (Savillex) along with a stir bar (30 mm, VWR). The mixture was then stirred while capped for 24 h. The sample was then removed and washed five times with water (~50 g water per g sample) via vortex mixing (VWR) followed by centrifugation (Beckman Coulter Allegra X-30R, 133 Hz for 360 s, 50 cm^3 centrifuge tubes) and dried overnight in a gravimetric oven held at 363 K. Once dry, the sample was calcined in a tube furnace (Thermo Scientific, Lindberg Blue M) at 823 K (0.0167 K s^{-1} ramp) for 8 h, in 1.67 cm^3 s^{-1} of house air.

2.2.4 Synthesis of MPC/FAU and MPC/C

To synthesize MPCs deposited on the external surfaces of FAU crystallites, 0.5 g of uncalcined Na/FAU, 200 cm^3 of acetone (VWR, 99.5%), and the desired mass of phthalocyanine was added to a 250 cm^3 PFA jar (Savillex) along with a stir bar (30 mm, VWR). For MPC/C, 0.5 g of Carbon Black Pearls (Cabot) was used instead. The mixture was stirred uncapped in a fume hood at ambient temperature to evaporate the acetone. Once dry, the resulting powder was collected and stored in a scintillation vial. Samples prepared via this route are termed "MPC/FAU" for the remainder of this article.

2.2.5 Synthesis of Si-xerogel

Si-xerogel was synthesized according to a modified procedure from literature.[4] First, 20 cm^3 of 0.1 M hydrochloric acid (HCl) were prepared by dilution from concentrated HCl (37%, Sigma Aldrich) with ultrapure water. Then, 2.28 g of 0.1 M HCl were added to a 250 cm^3 PFA jar (Savillex) along with 26.896 g of ultrapure water, 20.72 g tetraethyl orthosilicate (TEOS, 98%, Sigma Aldrich), and a stir bar (30 mm, VWR). This mixture was stirred for 2 h to homogenize the mixture. After stirring, 1 M ammonium hydroxide (prepared from 28% NH_4OH, Sigma Aldrich)

was added dropwise with a disposable glass pipette until the solution became a gel-like solid (typically ~68 drops). The stir bar was then removed, and the gel was dried overnight. The gel was then washed with ultrapure water by repeated vortex mixing and centrifugation until the pH of the supernatant remained constant (typically ~5.1). The sample was then treated in flowing air in a tube furnace (Thermo Scientific, Lindberg Blue M) at 823 K (0.0167 K s^{-1} ramp, held at 823 K for 10 h) in 3 cm^3 s^{-1} g^{-1} of flowing air.

2.2.6 Synthesis of Cobalt Nitrogen-Doped Carbon (Co-N-C)

Co-N-C was synthesized according to the procedure previously reported by Whitcomb et al.[19] Cobalt nitrate hexahydrate (0.5 g, Alfa Aesar, 97.7%) was dissolved in 10 cm^3 of house deionized water and added to a solution of 0.611 g of 1,10 phenanthroline (Sigma Aldrich, ≥ 99%) in 15 cm^3 of ethanol (Sigma Aldrich, > 99.9%) before stirring for 20 min at 353 K. The mixture was then added dropwise into a slurry of Carbon Black Pearls (Cabot) in 0.1 M NaOH (Fischer Scientific, 97.6%) and stirred for 2 h at 353 K. The solids were then separated by vacuum filtration and washed with 2000 cm^3 of house deionized water, then dried overnight in a static oven (Fisher Scientific, Isotemp 516G) at 343 K. The dried sample was then impregnated with 0.5 g dicyandiamide (TCI, > 98%). The mixture was then stirred in acetone (Alfa Aesar, 99.5%) at 329 K for 12 h and then dried by evaporation to ambient on the benchtop.

Once dry, the sample was thermally treated in a tube furnace (Thermo Scientific, Lindberg Blue M) at 973 K (0.0167 K s^{-1} ramp) for 2 h, in 1.67 cm^3 s^{-1} Helium (Airgas, 99.999%). The sample was then acid washed to ensure the removal of nanoparticles, in 250 cm^3 of 1 M HCl (VWR, 36.5-38%) at room temperature for 12 h. The acid-washed Co-N-C was then vacuum filtered and washed with 300 cm^3, then dried overnight at 343 K. The dried catalyst was then thermally treated

again in a tube furnace at 673 K (0.0167 K s^{-1}) for 2 h, in a H_2/He mixture (1.67 cm^3 s^{-1} total flow; 101 kPa total pressure; 5 kPa H_2, Airgas, 99.999%; balance He) to yield the final Co-N-C catalyst.

2.2.7 Synthesis of PdAu on SiO_2 by Strong Electrostatic Adsorption

PdAu (1:5) was synthesized according to previous literature[32] as a comparison material. First, a precursor solution was made with a salt of each metal. For gold, 1 cm^3 of 1,2-ethanediamine monohydrate (Sigma Aldrich, ≥ 99.5%) in 5 cm^3 of diethyl ether (Aldon Corp, reagent grade) were added to a solution of 1.0 g $HAuCl_4$ (Sigma Aldrich, ≥ 99.9%) in 10 mL of diethyl ether. The solution was then diluted with 2.8 cm^3 of Millipore water (18.2 MΩ). Then 20 cm^3 of ethyl alcohol (Electron Microscopy Sciences, ≥ 99.9%) were added to precipitate out a solid. The recovered solid was then dissolved again in 2.8 cm^3 of Millipore water, and reprecipitated with 15 cm^3 of ethyl alcohol. This yielded a solution of gold bis-ethylenediamine (AuBen). To make the Pd precursor solution, 0.002 g of tetraamminepalladium (II) nitrate (PdTAN) (Strem Chemicals Inc, 5.0% Pd) was dissolved in 20 cm^3 of Millipore water.

100 ppm solutions were made of AuBEN and PdTAN using the precursor solutions and Millipore water. The pH of each solution was adjusted using sodium hydroxide (97%, Sigma Aldrich) and hydrochloric acid (Sigma Aldrich, 37%) to achieve a pH of 10.5. 150 cm^3 of the pH-adjusted AuBEN solution and 18.6 cm^3 of the pH-adjusted PdTAN solution were stirred with 0.93 g of Si-xerogel for one hour. The wet powder was then dried at room temperature in darkness for 48 h. The sample was then reduced at 673 K for 1 h (0.083 K s^{-1} ramp, flow 4.17 cm^3 s^{-1} of 20% H_2 in He).

2.3 Catalyst Washing Tests

2.3.1Vortex Washing Procedure

"Unwashed" samples were split between two centrifuge tubes (VWR, 50 cm^3), with ~200 mg of sample per tube. Each tube was then filled with ~40 cm^3 of solvent. The tubes were then manually held on a vortex mixer and mixed for 20 s. The solids were separated from the solvent by centrifugation (8000 rpm for 360 s), and the resulting supernatant decanted. This process was repeated for 10 wash cycles with pyridine (Beantown Chemical, 99%), followed by four wash cycles with acetonitrile (VWR, ≥ 99.5%), and finally one more wash with water (ultrapure, Elga Purelab Flex). Samples were then dried overnight in a vacuum oven (Thermo Scientific, Lindberg Blue M, ~ 10 Torr) at 363 K to obtain a "washed" sample.

2.3.2 Soxhlet Extractor Washing Procedure

"Unwashed" samples were added to a glass fiber thimble (GE Life Sciences, 0.8 μm pore openings), and this thimble was placed inside a glass thimble (Chemglass, 60 μm pore openings). This two-thimble assembly was then placed in a Soxhlet extractor (Chemglass, CG-1368-02). The attached RBF was filled with 200 cm^3 of solvent, and the condenser was cooled with ambient temperature tap water. The exterior of the Soxhlet extractor was covered with fiberglass insulation (Refractory Engineers INC, DBS8.524) and aluminum foil, and the RBF was placed in a heated oil bath. Each sample was washed with three solvents for a total of 72 h: 24 h in acetone (VWR, 99.5%) heated to 353 K, 24 h in pyridine (Beantown Chemical, 99%) heated to 433 K, and 24 h in acetonitrile (VWR, ≥ 99.5%) heated to 393 K. Samples were then dried overnight in a vacuum oven at 363 K (~10 Torr) to obtain a "washed" sample.

2.3.3 Individual Solvent Washing Test

$CuPCF_{16}$/FAU was used to compare the washing ability of different solvents via vortex washing. For each solvent, 400 mg of sample was split between two centrifuge tubes. Each tube was then filled with ~40 cm^3 of the solvent. The tubes were then placed on a vortex mixer and mixed for 20

s. A centrifuge was used to separate the solids from the liquids, and the resulting supernatant was decanted. Some of the supernatant was saved after each wash and used to collect a transmission UV-Vis spectrum. Each supernatant was filtered using 0.2 μm pore size PTFE filter tips (VWR). Next, 2 cm^3 of the filtered supernatant were pipetted into a cuvette (Shimadzu, quartz, 10 mm) to collect the absorbance spectra from 300 to 800 nm at medium speed (1.97 nm s^{-1}) using a Jasco V-780 UV-VIS spectrometer. The maximum absorbance of each wash (centered between 670-690 nm) was plotted as a function of the number of washes. These results are reported in Figure S.1. This procedure was repeated for acetone (VWR, 99.5%), acetonitrile (VWR, ≥ 99.5%), dichloromethane (DCM) (Sigma Aldrich, 99.8%), dimethyl sulfoxide (DMSO) (Sigma Aldrich, 99.7%), and pyridine (Beantown Chemical, 99%).

2.3.4 Consecutive Washing Test

$CuPCF_{16}$/FAU was washed with water five times via vortex mixing and centrifugation to remove impurities, then washed with pyridine until the color of the supernatant remained unchanging throughout multiple washes; this required 23 pyridine washes. After washing with pyridine, the same solid was washed twice with DMSO, acetonitrile, acetone, and ultrapure water consecutively to determine if these solvents would remove any MPC that remained after washing with pyridine. Transmission UV-Vis spectra were collected using the same procedure described in §2.1.3.1. These results are reported in Figure S.3. The obtained solids were collected and placed in a vacuum oven to dry overnight at 363 K (~10 Torr).

2.4 Phthalocyanine Solubility Study

The solubility of different phthalocyanine complexes was probed using a modified procedure from Raja et al.[24] An aqueous solution of NaOH (97% Sigma Aldrich) of pH 12.8 was prepared in a 60 cm^3 PFA jar (Savillex) to replicate synthesis conditions. Then, 0.060 g of PC were added, and this mixture was stirred for 24 h. The solution was then heated to 363 K for 2 h, and the resulting hot slurry was centrifuged to separate any undissolved PC. The supernatant was decanted, and the remaining solids were dried overnight at 363 K in static air in a drying oven, and then weighed to determine the amount of PC dissolved.

2.5 Catalyst characterization

2.5.1 Powder X-ray Diffraction (XRD)

XRD patterns were collected on all hydrothermally synthesized zeolite samples to confirm the faujasite crystal structure and monitor for impurities of other zeolite phases. A Rigaku Miniflex II diffractometer with a low-background powder sample holder (Rigaku, 5 mm diameter, 0.2 mm depth) was used. Diffraction patterns were collected between 2-theta angles of 4-40˚ at a speed of 0.015˚ s^{-1} with a 0.1˚ step size.

2.5.2 N_2 adsorption

The micropore volumes of Na/FAU and MPC@FAU samples before and after washing were obtained by collecting N_2 adsorption isotherms at 77 K using a Micromeritics ASAP 2020. Samples were degassed at 623 K for nine hours (0.167 K s^{-1} ramp rate). The average micropore volume was determined by a semi-log derivative analysis. From a plot of $\partial(V_{ads}/g)/\partial(\log(P/P_0)$ vs. log (P/P_0), the micropore filling transition can be identified as the first maximum, with the end of micropore filling attributed to the first minimum after the first maximum.[33] The volume of adsorbed liquid nitrogen was obtained by multiplying the volume of adsorbed N_2 at the end of the

isotherm by the liquid molar density of N_2 (0.029 mol cm^{-3}). This procedure was used to calculate the micropore volumes reported in Table S.1.

2.5.3 Inductively Coupled Plasma Optical Emission Spectroscopy (ICP-OES)

The elemental composition of each sample was determined by ICP-OES after dissolving each sample in hydrofluoric acid (HF, VWR, 48-51%. (*Note: care should be taken when handling concentrated HF!).* Spectra were collected using a Perkin Elmer Optima 8300 instrument. Six calibration standards were made to calibrate the instrument for each element, with each standard containing an equal concentration (in ppm) of each element ranging from 0.1-25 ppm in 2 vol% nitric acid (diluted from 70%, Sigma Aldrich). 1000 ppm stock solutions in 2 vol% nitric acid were used to prepare these standards (Sigma Aldrich, TraceCERT). Due to significant downtime with this system, some samples were quantified using ICP mass spectrometry (ICP-MS using a Perkin Elmer Elan 6100 ICP-MS). Solutions were prepared using the same chemicals listed above.

2.5.4 Diffuse Reflectance Ultraviolet-Visible Spectroscopy (DRUV-VIS)

Ex situ DRUV-VIS spectra were collected in reflectance mode using a Shimadzu UV3600Plus spectrophotometer with a Harrick Praying Mantis Diffuse Reflection accessory (DRP–XXX) across the spectral range 190–900 nm with a scan rate of 1.97 nm s^{-1} and one nanometer resolution. Barium sulfate (Sigma Aldrich, 99%) was used as a 100% reflectance baseline for each spectrum. Reflectance measurements were converted to Kubelka-Munk absorbance units[34, 35] using Equation 1.

$$F(R) = \frac{(1-R)^2}{2R} \qquad \text{(eq. 1)}$$

In situ DRUV-VIS spectra were collected by replacing the sample stage with a Harrick high temperature reaction chamber (HVC–VUV). Samples were heated to 573 K in increments of 100

K in 8.33 cm^3 s^{-1} g^{-1} He (Airgas, 99.999%) using a Watlow EZ-Zone temperature controller, with a scan taken at each increment (range 190-900 nm with a scan rate of 1.97 nm s^{-1} and one nanometer resolution). The temperature was held at 573 K for one hour, and a scan was taken every 600 s.

2.5.5 Electron Paramagnetic Resonance (EPR) spectroscopy

EPR spectra were recorded on a Bruker-ESP 300-10 spectrometer at 77 K in a liquid nitrogen immersion dewar. A rectangular cavity operating at X-band (ca. 9.6 GHz) was used. Approximately 50 mg of sample were placed in a 3 mm quartz sample tube which had been sealed at the bottom. The top of the sample tube was plugged with glass wool to prevent the fine zeolite powders being expelled from the tube upon warming. A modulation frequency of 100 kHz was used, and the amplitude of the modulation and microwave power were adjusted to give the highest resolution. Simulations of the experimental spectra were carried out using Easyspin.[36]

2.5.6 X-ray Absorption Spectroscopy

X-ray absorption near edge structure (XANES) and extended X-ray absorption fine structure (EXAFS) data were collected at beamline 2-2 at the Stanford Synchrotron Radiation Laboratory (SSRL) at SLAC National Laboratory. For *ex situ* experiments, samples were pressed into pellets and sealed in Kapton tape. Due to the low weight loadings of each metal present in the MPC@FAU samples, fluorescence measurements were taken with either a PIPS diode or a germanium detector. *In situ* samples were pelleted and sieved to be between 180-250 μm, then loaded into a 1 mm o.d., 0.99 mm i.d. quartz capillary tube (Hilgenberg) with quartz wool (Sigma Aldrich) plugs at either side to keep the sample in place. Samples were then heated to 573 K (0.167 K s^{-1} ramp rate) under flowing He (0.33 cm^3 s^{-1}). Spectra were collected at ambient temperature before and after heating

in order to compare the EXAFS data at constant temperature. Data were collected using either continuous XAS and WebXAS software.

Ex situ XANES data for $CoPCF_{16}$@FAU, $CuPCCl_{16}$@FAU (in Figure S.58), $CrPCCl_{16}$@FAU, $FePCCl_{16}$@FAU (in Figure S.58), $MnPCCl_{16}$@FAU, $NiPCCl_{16}$@FAU, and $ZnPCCl_{16}$@FAU as well as *in situ* XANES data for $CuPCCl_{16}$@FAU were collected at the National Synchrotron Light Source (II) at Brookhaven National Laboratory on beamline 8-ID. *Ex situ* samples were loaded into 1.8 mm i.d. polyimide capillary tubes (Cole–Parmer) and sealed at both ends with Play-doh (Hasbro). *In situ* samples were loaded into the same polyimide tubes but were sealed on both ends with quartz wool pads. To simulate the pretreatment that would take place before reaction, samples were heated to 573 K (0.167 K s^{-1} ramp rate) under flowing He (0.167 cm^3 s^{-1}). Spectra were collected before, during, and after heating to observe any differences that may arise die to the catalyst pretreatment. For *operando* studies, samples were held at 298 K under reaction conditions (0.33 cm^3 s^{-1} total: 4.0 kPa CO, 30.4 kPa O_2, balance He) while taking scans to observe changes in the metal centers over time. After a He purge for two hours, samples were then treated *in situ* with CO (0.33cm^3 s^{-1} total: 4.0 kPa CO, balance He) and subsequently in pure O_2 (0.33 cm^3 s^{-1}) while taking scans. All analyses were performed with the Demeter software suite.

2.5.7 Fourier Transformed Infrared (FTIR) Spectroscopy

FAU samples were pressed into self-supporting wafers (~0.030 g, 1.8 cm diameter) and loaded into a Harrick high temperature transmission FTIR cell (HTC-3-NI8). Spectra were collected using a Thermo Scientific Nicolet 4700 FTIR spectrometer across the spectral range 400-4000 cm^{-1} with a resolution of 2 cm^{-1}. Each reported spectrum is the average of 64 scans. For *in situ* FTIR experiments, the cell was heated in increments of 50 K from 298-728 K using a Watlow EZ-Zone

temperature controller, and three spectra comprised of the average of 64 scans were collected at each setpoint (over ~720 s).

The same pretreatment protocol used for oxidation trials (Section 2.6) was used for *operando* FTIR experiments (temperature ramp 0.167 K s^{-1} to 573 K, hold for 3600 s). Samples were then cooled to 298 K via radiative heat transfer to ambient (over a period of ~ 3600 s), then the reactant feed for CO oxidation was introduced (0.83 cm^3 s^{-1} total: 4.0 kPa CO, 30.4 kPa O_2, 4.0 kPa N_2 (internal standard), balance He, 101.3 kPa total pressure). Spectra were collected periodically and recorded along with the corresponding gas chromatograph (GC) injections to quantify the contents of the effluent stream. The GC used was an Agilent 6890N GC equipped with a thermal conductivity detector and HP-PLOT-Q (30 m, 0.32 mm, 20 μm, Agilent) and CP-molsieve 5A (25 m, 0.35 mm, 30 μm, Agilent) columns. The Plot-Q and molsieve columns were connected in series, with a switching valve in between, in order to separate CO_2 from CO, O_2, and N_2, and when necessary, to trap co-fed H_2O to prevent it reaching the molsieve column. The fractional conversion of CO was calculated using Equation 2.

$$\text{Conversion} = \frac{CO_{in} - CO_{out}}{CO_{in}} \qquad \text{(eq. 2)}$$

The carbon balance was calculated using Equation 3.

$$\text{Carbon balance (\%)} = \frac{CO_{out} + CO_{2,out}}{CO_{in}} \times 100 \qquad \text{(eq. 3)}$$

2.6 Catalytic testing

2.6.1 Packed bed reactor tests

Powder samples were pressed into pellets, ground in an agate mortar and pestle (VWR, 89037-486), and sieved (W.S. Tyler, #60, #80) to retain particles with diameters between 180-250 μm. After sieving, 0.050 g of solid was loaded into a 10.16 cm long, 9.53 mm o.d. (6.76 mm i.d.) quartz tube. The quartz tube was sealed with ultra torr fittings (Swagelok) and surrounded by a custom fabricated brass cube (5.08 cm edge length) equipped with resistive heating cartridges (Omega, CIR-2050, 120V). This apparatus was housed within a gravimetric oven (Quincy 10GC) and a K-type thermocouple (Omega) housed within a 3.18 mm o.d. quartz thermowell sealed with ultra torr fittings (Swagelok) was used to monitor and control the catalyst temperature (see reactor diagram in the Supporting Information, Section S.5). Samples were pretreated by a temperature ramp of 0.167 K s^{-1} to 573 K, followed by maintaining a constant temperature of 573 K for one hour, all under 0.83 cm^3 s^{-1} He flow. The catalyst bed was then cooled to 298 K via radiation to ambient (over a period of ~ 3600 s), then the reactant feed for CO oxidation was introduced (0.83 cm^3 s^{-1} total: 4.0 kPa CO (NexAir, 99.9%), 30.4 kPa O_2 (Airgas, 99.994%), 4.0 kPa N_2 (internal standard, Airgas, 99.999%), balance He (Airgas, 99.999%)). All He passed through a moisture and oxygen trap (Matheson, SEQPURILIOMT1). All N_2 and O_2 passed through a moisture trap (Matheson, SEQPURILMT1). The CO feed was passed through a moisture and oxygen trap (Matheson, SEQPURILIOMT1) followed by a Cu trap (Cu turnings in a Swagelok transport cylinder, 316L-HDF4-150) held at 593 K by resistive heat tape and a temperature controller (J-Kem Scientific Model 150), to remove undesired carbonyls that may be present in the concentrated CO cylinder or supply lines. The composition of the reactor effluent was monitored until the rate of CO_2 production decreased to zero. Conversion was calculated using equation 2 and carbon balance was calculated using equation 3. The carbon balance closed to 100±5% for all data reported in this manuscript. CO_2 site time yields were calculated using equation 4, where $\dot{m}$ is the CO_2 flow rate

in $cm^3\ min^{-1}$, m_{cat} is the mass of catalyst loaded in the reactor, P is the pressure (with units of Pa), R_g is the ideal gas constant, and T is the temperature (with units of K).

$$STY = \frac{\dot{m}}{m_{cat}}\left(\frac{1\ m^3}{1\times10^6 cm^3}\right)\left(\frac{1\ min}{60\ s}\right)\left(\frac{P}{R_g T}\right) \quad \text{(eq 4)}$$

The reactor feed was then changed to flow only He (0.83 $cm^3\ s^{-1}$) at 298 K and left under that condition for 12-72 h. After this He treatment, flow of the reactant stream was resumed.

Site time yields for CO_2 formation were quantified by gas chromatography as described in section 2.5.7. These site time yields were then normalized per gram of catalyst and plotted against time on stream. An exponential decay was then regressed against the resultant curves in Microsoft Excel. These regressions were then used to calculate the site time yield at time zero (initial site time yield).

2.7 Computational Methods

Computational methods used in this study are briefly described here. For additional computational details, please refer to the Supplementary Information, Section S.2.

2.7.1 Geometry of FAU-encapsulated MPCs

As a starting point to provide insight into the geometry of the encapsulated PCs, we carried out molecular dynamics (MD) simulations on perfluorinated (i.e., fluorine as periphery ligand, see Figure S.37) ZnPC encapsulated in FAU zeolite. Zn was chosen as metal center due to the closed shell electronic structure of ZnPC. The MD simulations were used to generate possible conformations of the PC within the FAU framework. The simulations were performed at the GFN-FF level of theory using the xTB program (version 6.4.1).[37, 38]

Final geometry optimizations of the FAU-encapsulated $ZnPCF_{16}$ were carried out using an additive quantum mechanical/molecular mechanical (QM/MM) approach where the QM region comprised the $ZnPCF_{16}$, and the MM region was further partitioned into two regions: a frozen MM region in which zeolite atoms were held fixed to ensure a bulk-like structure far from the QM region, and an active MM region, a spherical region centered around MPC, in which zeolite atoms were allowed to move during the geometry optimization.

Defective FAU structures around the $ZnPCF_{16}$ were created by removing silicon and oxygen atoms that were within 2 Å away from the F atoms and terminating dangling Si or O atoms with -OH or -H, respectively. The geometries were then relaxed using the same QM/MM approach described above and single point calculations performed as discussed previously.

2.7.2 Binding Free Energy (BFE) Calculations

For the binding free energy calculations, each MPC (M = Cr, Mn, Fe, Co, Ni, Cu, Zn) was modeled as a single unit in vacuum. All DFT calculations were performed at the PBE-D3(BJ)//def2-TZVPP/PBE-D3(BJ)/def2-SVP[39, 40] level of theory using the GAUSSIAN 16 program suite within a spin unrestricted formalism (UDFT).

2.7.3 Reaction Mechanism Calculations

All geometry optimizations, transition state calculations, and frequency calculations were carried out using DFT at the PBE-D3(BJ)/def2-TZVPP//PBE-D3(BJ)/def2-SVP[39-41] level of theory as implemented in the GAUSSIAN 16 program suite within a spin unrestricted (UDFT) formalism

2.7.4 UV-Vis and XAS Calculations

We have also calculated the UV-Vis and XAS spectra of the MPCs in vacuum to provide computational validation of experimental UV-Vis and XAS spectra. For the UV-Vis calculations, the adsorption spectra (first 40 excited states) of each MPC was calculated using the optimized geometries obtained during the binding energy calculations at the ωB97X-D/def2-SVP level of theory [40, 42] using the GAUSSIAN 16 program suite. All XAS calculations were performed using the FDMNES code (Release 2022-02-24).[43, 44]

3. Results and discussion

3.1 Solubility and Washing Tests

In order to determine whether MPCs would be soluble during zeolite synthesis, a basic pH solution was used to simulate the pH of the zeolite synthesis gels. MPCs of varied peripheral substituents were stirred in this solution, and the amount of MPC dissolved determined (Figure 1). Replacing the peripheral hydrogens of phthalocyanine with halogens increased solubility, with the solubility of perchlorinated phthalocyanine the greatest. These results are in agreement with previous studies by Raja and Ratnasamy.[24] It is possible that MPCs are not fully dispersed in zeolite synthesis gels, and the encapsulated species are in fact agglomerates of greater than one MPC. MPC@FAU samples synthesized with perchlorinated phthalocyanines generally had higher metal loading weight loadings, as shown in the results from ICP-OES reported in Table S.1.

Equipped with knowledge of which MPCs were most likely to be soluble and thus able to be encapsulated during hydrothermal synthesis, we next aimed to confirm that we would be able to remove undesired MPCs adsorbed on the exterior of FAU crystals via washing with various

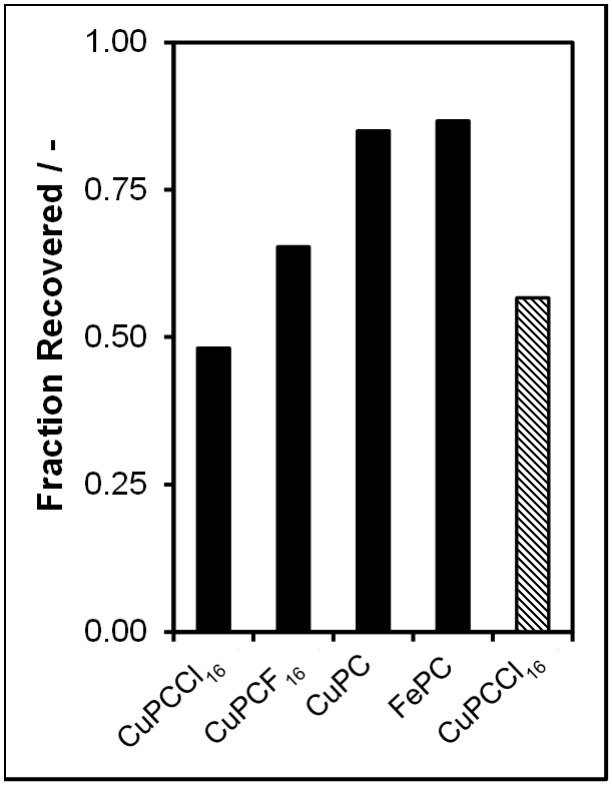

Figure 1: Results of solubility studies of various metal phthalocyanines (0.060 g MPC in 10 cm^3 water, with pH controlled to ~12.8 via addition of NaOH). Striped bar shows results from Raja and Ratnasamy.[35]

solvents. $CuPCF_{16}$/FAU was washed with a series of solvents using a vortex mixer to determine which solvent was the most effective at removing MPCs on the external surface of FAU. We collected UV-Vis spectra and measured the maximum absorbance (centered between 670-690 nm) for each supernatant solution as a function of the number of wash cycles performed. Pyridine was the most effective solvent for removing MPCs from the external surface of FAU, as the UV-Vis absorbance after each wash was an order of magnitude greater than those measured after washing with other solvents (DMSO, acetone, acetonitrile, DCM). These results are reported in Figure S.2.

The first 10 wash cycles with pyridine removed the majority of the MPC from the external surface of FAU. After the second wash, the maximum absorbance was 0.85, while the maximum absorbance from the supernatant after the tenth wash was 0.12. The decrease in maximum absorbance was minimal for wash numbers 11-23. The supernatant from wash 11 had a maximum absorbance of 0.09, while the supernatant from the twenty third wash had a maximum absorbance of 0.02. Based on a lack of blue color between solvent washes (either visually or based on UV-Vis spectra) with any of the solvents after the 23 washes with pyridine, these solvents did not remove any MPC from the FAU surface. In light of this experiment, a uniform washing procedure was developed: five washes with water, ten washes with pyridine, four washes of acetonitrile, and one water wash. The purpose of the acetonitrile washes was to remove any residual pyridine. Due to the large number of vortex washes required to remove all external MPCs, a Soxhlet extractor was used to allow samples to be washed continuously with no user interaction. Soxhlet washing samples for 24 hours each sequentially in acetone, pyridine, and acetonitrile was found to remove all MPC from $CoPCF_{16}$/FAU (see Figure S.9.b).

3.2 Structural characterization of catalysts

All catalyst samples were characterized by XRD, N_2 adsorption, FTIR, and ICP-OES and *in situ* DRUV. Example XRD patterns are reported in Figure S.4. These show the expected diffraction peaks for FAU zeolites, with minor impurities for GIS ("Zeolite P1", observable by diffraction peaks at 17.6°, 21.6°, and 28.0° 2θ) that have been reported previously.[45, 46] When samples were prepared as reported previously (with sodium aluminate and Ludox AS-40 and a crystallization temperature of 338 K[46]), the resultant materials were amorphous (Figure S.5). Attempts to vary the Si:Al ratio in the gel and crystallization temperature with this reagent blend inevitably led to mixtures of FAU, GIS, SOD, and LTA (Figure S.6). As a result, we adapted protocols from

Mintova and colleagues,[31] took guidance from Rimer and colleagues,[46] and ultimately used aluminum hydroxide at high gel Si:Al ratios in order to crystallize FAU with minimal phase impurities. However, increasing the Si:Al ratio of the synthesis gel also led to a decrease in the total yield of solid products (Figure S.8). The results of all structural characterizations are reported in Table 1.

N_2 isotherms are often used to determine micropore volumes of hydrothermally synthesized zeolites, as these are characteristic of each zeolite topology. However, for MPC@FAU

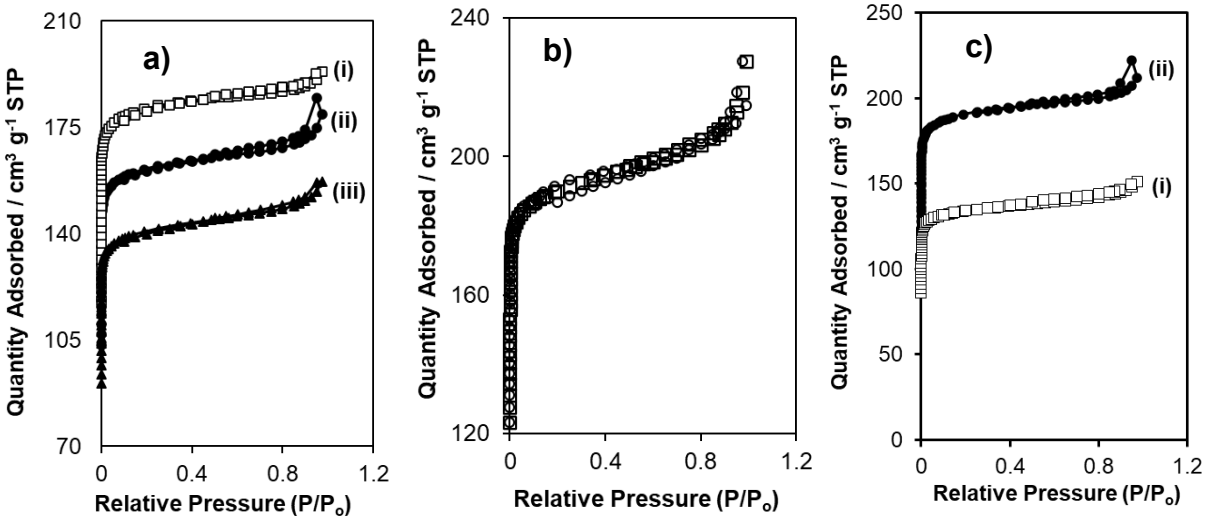

Figure 2. N_2 isotherms for various (a) Na/FAU and MPC@FAU samples: (i) Na/FAU, (ii) $CuPCCl_{16}$@FAU, (iii) $FePCF_{16}$@FAU; (b) Na/FAU before (circles) and after (squares) washing in Soxhlet extractor; (c) $CuPCF_{16}$@FAU before (i) and after (ii) calcination at 823 K for 8 h;

samples, lower micropore volumes than pristine Na/FAU zeolites are expected due to occlusion of micropore volume resulting from encapsulation of MPCs.[24] Indeed, micropore volumes were lower for MPC@FAU samples compared to phthalocyanine-free FAU (Figure 2a). Additional N_2 isotherms can be found in Section S.12. From these data alone, it is unclear whether the lower micropore volumes for MPC@FAU samples than Na/FAU can be attributed solely to the encapsulation of MPCs, as residual pyridine from the washing protocol may remain bound to residual Brønsted or Lewis acid sites in the zeolite. To probe the impact of pyridine from the

Soxhlet washing procedure, MPC-free Na/FAU was washed using the Soxhlet extractor, and its micropore volume compared to unwashed Na/FAU. As shown in Figure 2b, the Soxhlet washing procedure had no impact on the average micropore volume of Na/FAU. Additionally, after calcination of MPC@FAU at 823 K to remove any occluded MPCs the micropore volumes were consistent with that of FAU (Figure 2c). This suggests that our samples are indeed crystalline FAU with MPC occluded within the pores (see Figure 2 and Table S.1). ICP-OES measurements determined the M loadings shown in Table S.1.

The low metal loadings of these samples are due to the limited solubility of the phthalocyanine complex in the synthesis gel, which can be manipulated by changing the peripheral substituents of the metal phthalocyanines. For example, when the peripheral substituents of cobalt phthalocyanine were chlorine instead of fluorine, the metal weight loading of the washed sample from 0.018 to 0.026 wt%. These differences in metal loading are consistent with the findings of the solubility test (Figure 1). Transmission FTIR spectra of MPC@FAU samples (Figure S.10) show the presence of expected stretching bands for MPC complexes. These include C–H in aromatic (3047 cm^{-1}), C=C (1590 cm^{-1}), –N= (1507 cm^{-1}), pyrrole (1333 cm^{-1}), and isoindole (1480 cm^{-1}).[47] All FTIR stretches were of relatively low intensity consistent with the low weight loadings of each metal measured by ICP-OES.

DRUV measurements were used to confirm the presence of phthalocyanine complexes on FAU samples. The conjugated π-bonding system in phthalocyanine gives a characteristic peak in the 500-700 nm range known as the "Q-band."[48] The presence of these broad peaks in DRUV spectra of FAU samples indicates that the samples contain phthalocyanine from the synthesis gel for "unwashed" samples and that phthalocyanine remains after washing for "washed samples". DRUV spectra of $FePCCl_{16}$@FAU before and after washing are reported in Figure S.9a. DRUV

spectra of $CuPCF_{16}$/FAU after washing via Soxhlet extraction suggest washing procedure removes all external MPCs as Q band is removed (Figure S.9b) Computational simulations of these DRUV spectra (Figure S.62) predict shifts of the Q-band based on the identity of the peripheral ligand, but experimental spectra are not able to distinguish these shifts due to the breadth of the Q-band. Attempts to synthesize $CoPC(SO_3)_2$@FAU were deemed to be unsuccessful, as no Q-band was present in the DRUV spectra after washing. To prove that the encapsulated MPCs would be stable in the eventual pretreatment before reaction, we replicated this pretreatment with an *in situ* DRUV experiment (Figure S.9d) with $CuPCCl_{16}$@FAU. The Q-band was still present after heating to 573 K for one hour, indicating that the encapsulated MPCs remain intact after this pretreatment.

Having confirmed that the desired zeolite phases were formed, and that MPC complexes were present in the washed materials, we next used EPR and XAS to assess the oxidation states and bonding partners of the M centers present in MPC@FAU and MPC/FAU catalysts. XAS measurements are essential to probe whether the MPC complex is intact after encapsulation, as the UV-Vis spectrum of metal-free phthalocyanine also has a Q-band (Figure S.9c).

3.3 Characterization by EPR spectroscopy

EPR spectroscopy is sensitive to unpaired electrons in metal complexes, and some of the divalent MPCs are expected to be EPR active (copper,[49] cobalt,[50] manganese,[51] vanadyl[52]) others will be EPR silent (e.g., Fe(II)PC). Complicating analysis, oxidized forms containing for example, Fe(III) impurities or oxidized FePC complexes, are EPR active. The EPR spectra can be found in Section S.14. For copper, cobalt, manganese, and iron phthalocyanines, the observed EPR spectra are compatible with what would be expected from the metal phthalocyanine.

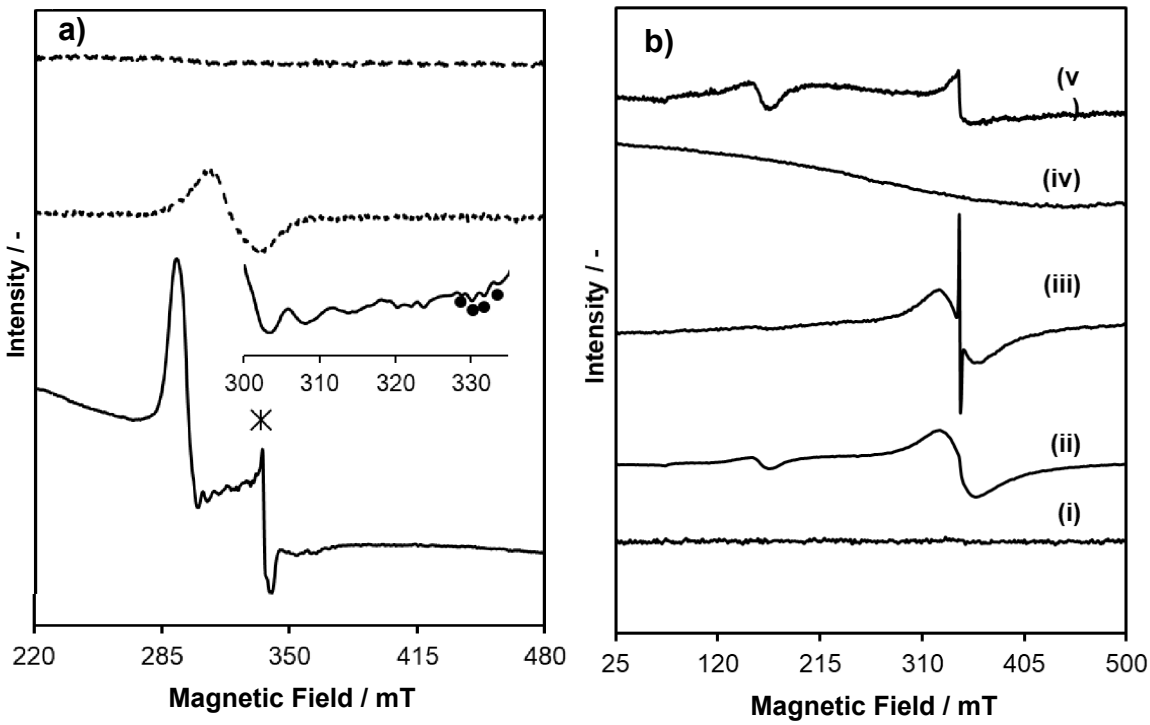

Figure 3. (a) CW-EPR X-band spectra (9.46 GHz) at 77K liquid N_2, amplitude modulation of 8G, mod freq. 100 kHz microwave power 21.20 mW of $CoPCF_{16}$@FAU, washed and dried (dashed); unwashed, in pyridine (dotted); and washed in pyridine (solid). The asterisk indicates a carbon centered radical around=2.0 often seen in cobalt phthalocyanines. The inset shows an expansion of the axial region, with a multiplet of ^{14}N peaks indicated by dots. **(b)** CW-EPR X-band spectra (9.67 GHz) at *T* 77K liquid N_2, amplitude modulation 5G, modulation frequency 100 kHz and microwave power 0.2114 mW of (i) 10 mM $Fe(II)SO_4$ in conc. H_2SO_4 (ii) 10 mM $Fe_2(III)(SO_4)_3$ in conc. H_2SO_4 (iii) 10 mM $Fe(III)PCF_{16}$ in conc. H_2SO_4 (iv)10 mM $Fe(II)PCF_{16}$ in conc. H_2SO_4 (sealed in 3 mm EPR tube after purification by freeze thaw pump in dichloromethane) (v) oxidation of 10 mM $Fe(II)PCF_{16}$ in 28 mM $NaIO_4$ in conc. H_2SO_4.

The cobalt phthalocyanine was particularly illuminating (Figure 3a), as in the as-prepared $CoPCF_{16}$ no EPR signal was observed. However, an unwashed sample dispersed in pyridine shows a broad spectrum consistent with low spin Co(II). Similarly, a washed sample dispersed in pyridine shows a well resolved, although weak spectrum, with a g-perpendicular feature at low field and a series of broad peaks at higher field consistent with axial hyperfine coupling from ^{59}Co. There are also some weaker features visible on the axial peaks (marked in the inset to Figure 3a) that suggest hyperfine coupling from nitrogen-14 from axial pyridine ligand or ligands, as reported by earlier workers for cobalt phthalocyanine.[53] These results are consistent with the cobalt perfluoro

phthalocyanine being in a high spin, S=3/2 state in the zeolite in the absence of pyridine, which gives a very broad spectrum not easily observed at 77 K. Addition of pyridine, which is a strong ligand, switches the complex into a low spin, S=1/2, spin state. From this it can be inferred that there is space inside the supercages of FAU for both a phthalocyanine and at least one axially bound pyridine. This also confirms that all pyridine is removed from the zeolites during the Soxhlet washing procedure, as the washed and dried sample in Figure 3 was exposed to pyridine during the Soxhlet extraction procedure, which we conclude was removed by the subsequent Soxhlet extraction in acetonitrile or the vacuum drying step (363 K).

The comparative study of Fe(II) and Fe(III) is shown in Figure 3b by EPR spectrum. Fe (II) is EPR inactive and thus gives a flat signal while Fe(III) is EPR active species and gives peaks at g = 4.31 and 2.01 respectively (See Figure 3b.ii). The distinct sharp peak g = 2.01 at 9.67 GHz in Figure 3b.iii for 10 mM Fe(III)PCF_{16} is assigned to carbon centered radicals, while for the same spectra the signal at g ~ 2.01 (broad spectra) is consistent with the superoxide ion bonded in an axial position to a central Fe- atom.[54] Figure 3b.iv is the resultant spectrum of Fe(II)PCF_{16} after purification by freeze-thaw-pump for 900 s (4 times) in vacuum using dichloromethane then mixed with conc. H_2SO_4 and sealed under vacuum in a 3 mm EPR tube. The EPR spectrum shows a flat line when Fe(III)PCF_{16} is reduced to Fe(II)PCF_{16} by driving off superoxide ion bound to the central Fe-atom. The same sample is then mixed with 28 mM $NaIO_4$, which would be expected to oxidize Fe(II) to Fe(III). Figure 4b.v shows the EPR spectrum after oxidation where the high spin is distinct at g = 4.31 while low spin at g = 2.01 are observed.

3.4 Characterization by X-ray Absorption Spectroscopy

K-edge X-ray absorption spectra were collected at BL2-2 at SSRL (Figure 4). For Cu-containing samples (Figure 4 a, b), characteristic pre-edge features in the XANES region can give insight into the oxidation state of the copper atoms due to their 1s-4p dipole-allowed transition.[55] This pre-edge peak is located at 8984 eV for a +1 oxidation state, and shifts to 8987 for the +2 oxidation state present in copper phthalocyanine.[55] XANES spectra of the $CuPCCl_{16}$ precursor and $CuPCCl_{16}$@FAU include the expected pre-edge feature at 8987 eV, indicating that CuPC present in the sample remains intact after occlusion in FAU. However, the XANES spectra for $CuPCF_{16}$@FAU includes a pre-edge peak at 8984 eV, indicating a +1 oxidation state. Since the $CuPCF_{16}$ precursor had the expected +2 oxidation state pre-edge feature, there is likely something else attached to the central metal atom that is causing this reduction of Cu or an undesired impurity species present (e.g., ion-exchanged Cu(I)). Cu EXAFS spectra were fit to crystallographic information framework files from previous literature obtained through the CCDC database.[56] $CuPCCl_{16}$ and $CuPCCl_{16}$@FAU were fit in the first coordination shell to coordination numbers of ~4, consistent with the four copper-nitrogen bonds in copper phthalocyanines. These first shell fits can be found in Figure 4 panels c and d.

For Fe-containing samples (Figure 4 panels e and f), XANES spectra include similar pre-edge features that give characteristic information about the oxidation state and geometry of Fe atoms. A pre-edge feature at 7113 eV is expected for a quadrupole-allowed 1s-3d transition characteristic of Fe(III), typically in a square pyramidal or octahedral geometry.[57] A peak at 7118 eV along the rising edge is characteristic of a 1s-4p transition of Fe atoms with a +2 oxidation state in square planar geometry.[57] The XANES spectra for $FePCF_{16}$@FAU, the $FePCF_{16}$ precursor, and Fe-FAU are reported in Figure 4c. All three spectra include a pre-edge feature at 7113 eV characteristic of Fe(III) with square pyramidal geometry.

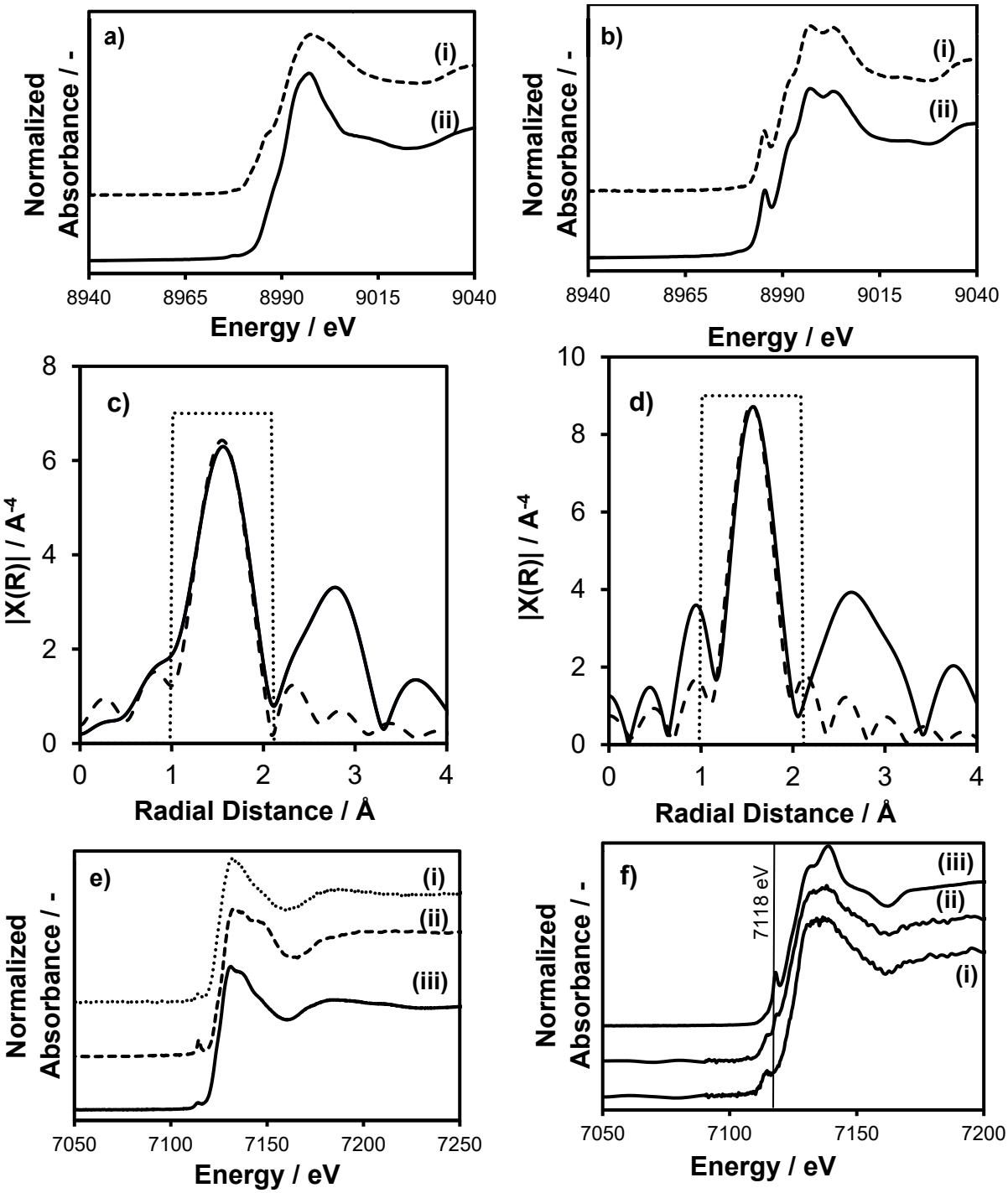

Figure 4. XANES spectra of various MPC, MPC@FAU, and M-FAU samples, offset vertically for ease of comparison: a) (i) $CuPCF_{16}$, (ii) $CuPCF_{16}$@FAU; b) (i) $CuPCCl_{16}$, (ii) $CuPCCl_{16}$@FAU; c) *Ex situ* EXAFS fit (dashed) of first coordination shell (dotted window) of $CuPCCl_{16}$ (solid) d) *Ex situ* EXAFS fit of first coordination shell of $CuPCCl_{16}$@FAU e) *Ex situ* spectra of: (i) Fe/FAU, (ii) $FePCF_{16}$@FAU, (iii) $FePCF_{16}$; f) *In situ* spectra of $FePCCl_{16}$@FAU (i) as prepared, (ii) post-heating, (iii) FePC from Sigma Aldrich for comparison, 7118 eV peak shown with vertical black line.

We hypothesized that the Fe may have remained in the phthalocyanine complexes, but that

oxygen or another ligand were axially bound to Fe resulting in an increase in oxidation state and loss of square planar geometry. We probed this by performing an *in situ* XAS experiment on $FePCCl_{16}$@FAU. After heating to 573 K in flowing helium and cooling to 298 K, we observed the peak at 7118 eV indicative of square planar Fe(II), indicating the removal of an axial ligand from the Fe atom and reduction from Fe(III) to Fe(II). Nevertheless, this reduction was incomplete. Further heating above 573 K may have fully reduced the Fe atoms, but the temperature range was limited by the sublimation temperature of the phthalocyanine complex (~673 K).[58]

For Co-containing samples, *ex situ* XANES data (Figure S.13a) show that $CoPCF_{16}$@FAU is distinct from CoO, however the signal to noise in the fine structure region is too low to fit (see Figure S.12). This is likely due to the low Co loading of this sample (see Table S.1). EXAFS data for $CoPCF_{16}$/FAU (Figure S.13b), however, fit to a $CoPCF_{16}$ geometry with a coordination number of 4.4 ± 1.2.[59] This is consistent with the four Co-N bonds present in MPC, but with the error in this measurement, it is possible that the coordination number is actually five. Possible ligands that may be bound to these metal centers are discussed in Section 3.7.

Operando XAS experiments on $CuPCCl_{16}$@FAU were conducted at beamline 8-ID at NSLS-II. No change in the XANES region was observed after heating to 573 K under He flow, similar to the pretreatment conditions before running CO oxidation (Figure S.11a). During *operando* XAS experiments, we observed a monotonic decrease in the intensity of the pre-edge peak during CO oxidation, as shown in Figure 5. A subsequent treatment in flowing He results in a monotonic increase in the intensity of the pre-edge peak nearly back to its original value. These results confirm that the Cu in the sample interacts with reactant gases and that whatever changes occur near the Cu center are reversible under He flow at ambient temperature. I*n situ* treatments of the sample

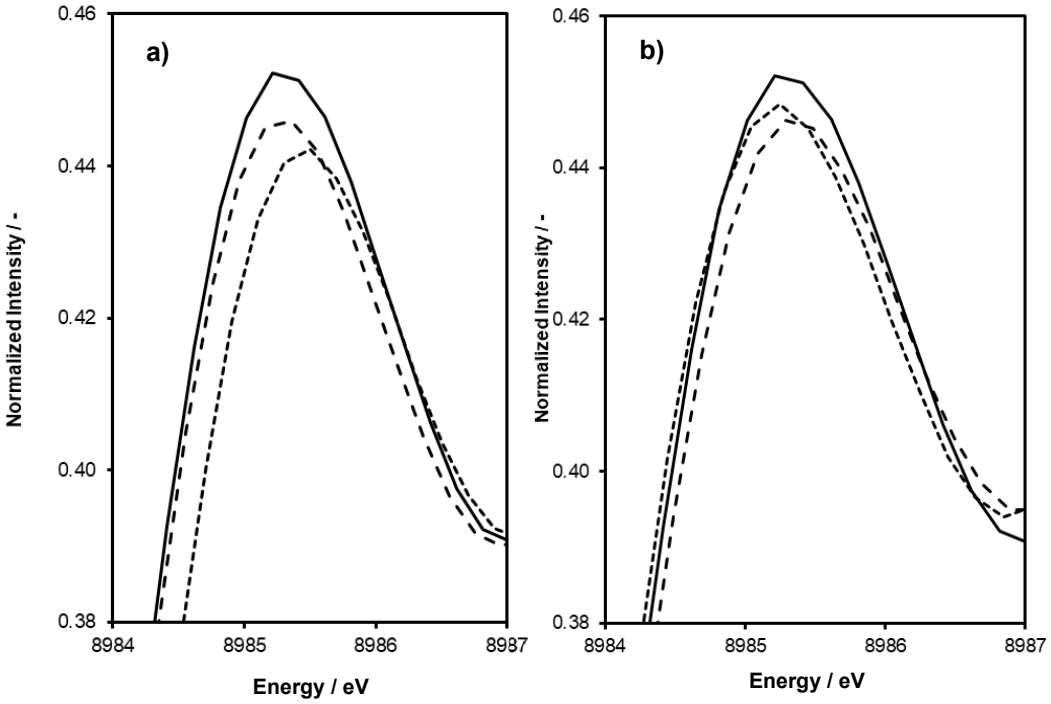

Figure 5. Cu K-edge XANES pre-edge feature of $CuPCCl_{16}$@FAU **(a)** during *operando* CO oxidation: before reaction (solid), after 1.2 ks of reaction (dashed) and after 8.4 ks of reaction (dotted). **(b)** During He treatment after 2.4 ks (dashed) and after 7.2 ks (dotted).

with pure O_2 (Figure S.11b) and 4% CO in He (Figure S.11c) suggest that adsorbed O_2 may be the cause of deactivation observed over $CuPCCl_{16}$@FAU, as a similar monotonic decrease was

observed during *in situ* treatment in pure O_2. Next, we report reactivities over MPC catalysts for CO oxidation with O_2 and other attempts to identify the source of deactivation on different MPCs.

3.5 CO oxidation with O_2

MPC@FAU samples were tested for CO oxidation with O_2 as a probe of their efficacy in aerobic oxidation reactions. Multiple reports of ambient temperature CO oxidation over Co-N_4-C[19] and CoPC@FAU[29] suggested these materials would be reactive even at ambient temperature. Consistent with these prior reports, $CoPCF_{16}$@FAU was one of the most reactive materials tested, as shown in Figures 6 and 7. $CoPCF_{16}$@FAU catalyst converted ~20% of the CO in the feed initially (4 kPa CO, 30 kPa O_2, 4 kPa N_2, balance He, 101 kPa total pressure, 130,000 h^{-1} WHSV, 298 K), followed by a decline in reactivity with time on stream. $MnPCCl_{16}$@FAU and $CuPCCl_{16}$@FAU were similarly reactive on a gravimetric basis but had lower initial STYs due to the increased solubility of perchlorinated MPCs relative to perfluorinated MPCs, which resulted in higher weight loadings of these MPCs encapsulated in FAU. Additional site time yield vs. time on stream data are reported in Section S.11, and the regressed exponential decays used to calculate initial gravimetric production rates are reported in Section S.12.

To ensure that the cause of deactivation was not an impurity in the system, we tested a different type of catalyst with a higher site density that is known to be active for CO oxidation. Bimetallic PdAu (1:5 Pd:Au molar ratio) nanoparticles supported on SiO_2 were tested for CO oxidation at 503 K under similar pretreatment and reaction conditions as those previously reported.[60] After some initial deactivation, the sample reached a steady state conversion of ~10%, which is consistent with the results reported by Xu et al. (see Figure S.14).[60] Based on these results, we

conclude that the deactivation to zero rate observed over MPC catalysts is inherent to the MPC active sites themselves, and not due to an artifact within our reactor system.

The reactivity of MPC@FAU samples could be regenerated by flowing He at ambient temperature for 24-72 h. An experiment testing different He treatment times (3 h, 24 h, 72 h) on the same sample of $ZnPCCl_{16}$@FAU found that each treatment time sufficiently regenerated the catalyst, with an average initial gravimetric production rate of $7.2 \pm 0.9 \times 10^{-6}$ mol g_{cat}^{-1} s^{-1} (Fig. S.41). The differences between the initial rates of these tests are within the error of different GC injections given the sensitivity of the extrapolation to initial time on the first measured rate. The STY was essentially invariant with reactor temperature (Figure 6a), which could result from the sensitivity of the initial rate determination to the timing of the first GC injection relative to the exposure of the catalyst to the reactant mixture (i.e., experimental uncertainty). However, it is also possible

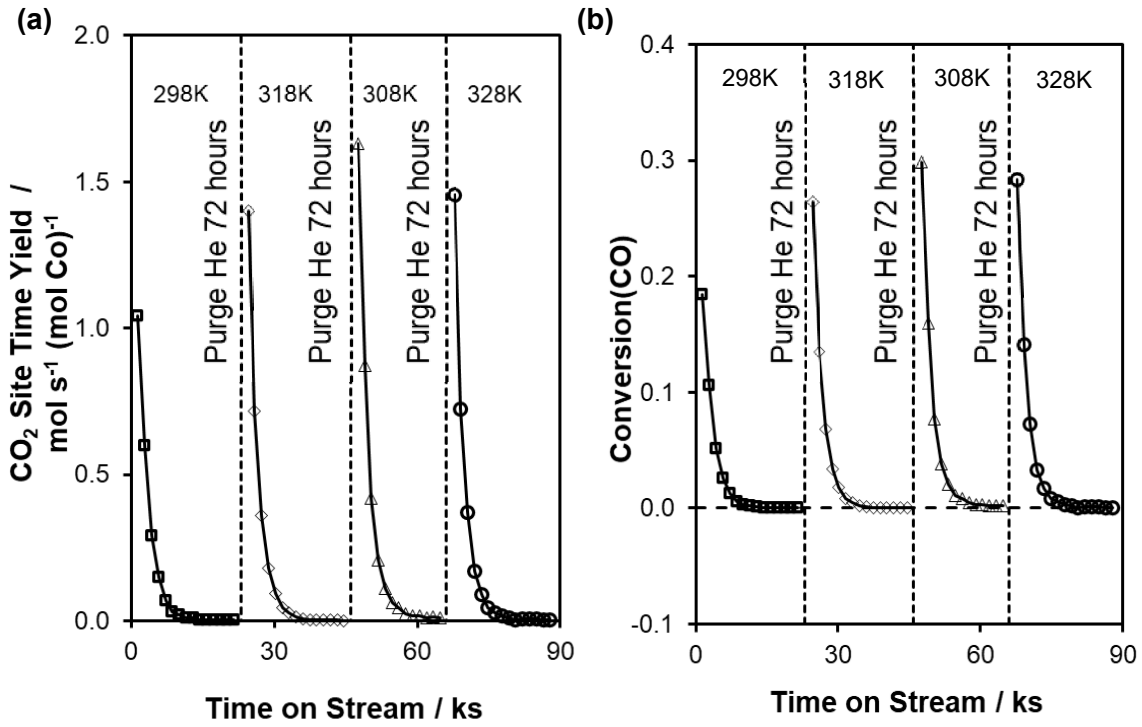

Figure 6. Results of CO oxidation with O_2 over $CoPCF_{16}PC$@FAU; (a) rate of CO_2 production, (b) CO conversion. Reaction conditions: Various T, 0.05 $g_{catalyst}$, 0.83 cm^3 s^{-1} total flow; total pressure 101 kPa; 4.0 kPa CO, 30.4 kPa O_2, 4.0 kPa N_2 (internal standard), balance He.

that this temperature range lies between two distinct kinetic regimes – one in which O_2 adsorption is rate determining and thus apparent activation energies are negative, and a higher temperature regime in which positive activation energies are observed, by analogy to recently reported results over Co-N_4-C materials.[19] We synthesized a batch of a recently reported[19] Co-N-C catalyst, and tested its CO oxidation activity at similar conditions. This Co-N-C had similar activation energy (Fig. S.22) and reactant reaction orders (Fig. S.23) to those reported by Whitcomb et al.[19] However, after initial deactivation, the Co-N-C sample was much more stable with time on stream compared to $CoPCF_{16}$@FAU. These results suggest that $CoPCF_{16}$@FAU reacts differently from Co-N-C, and that the activity and subsequent deactivation of $CoPCF_{16}$@FAU for CO oxidation is distinct from the behavior of Co sites in Co-N-C catalysts. Further kinetic studies of these materials at sub-ambient or elevated temperatures could further clarify this behavior, though given the

lengthy time for the inter-condition purge steps (~24–72 h) and our inability to operate at sub-ambient temperatures, those experiments were not included in the present study.

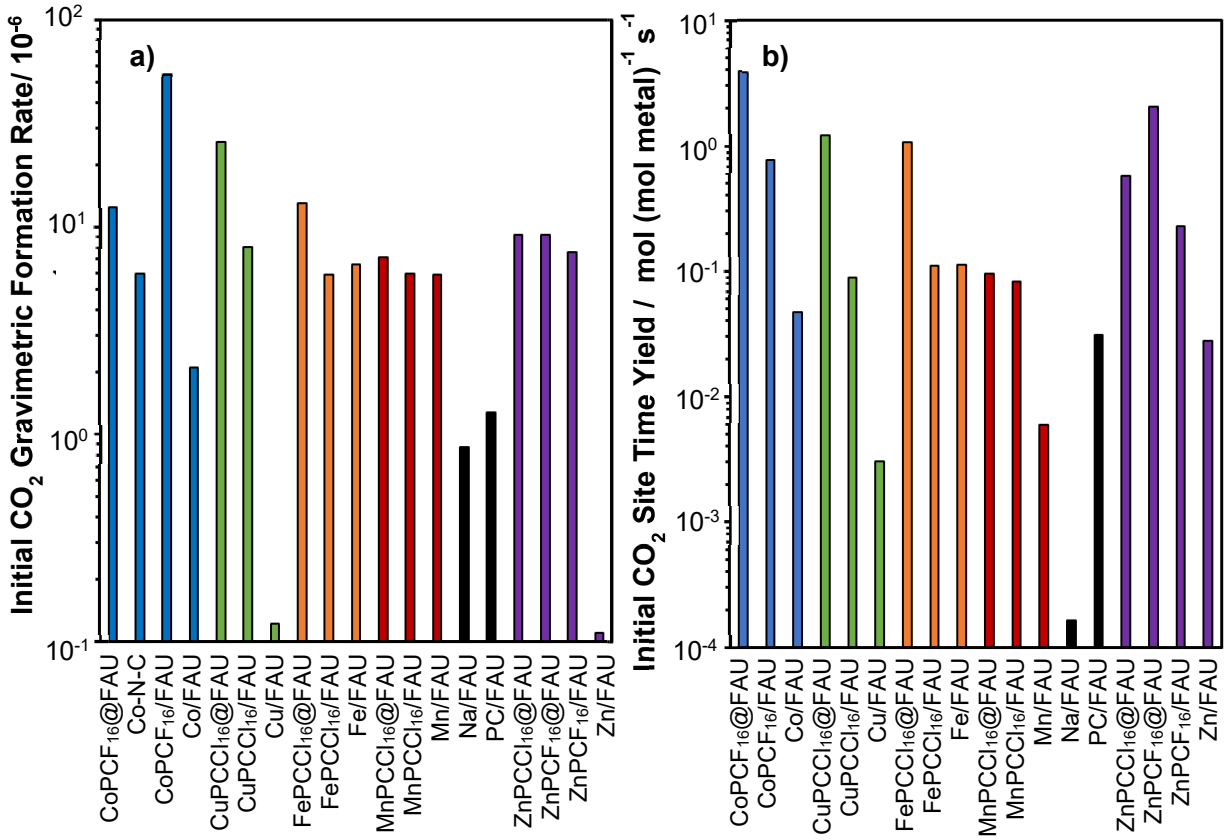

Figure 7. (a) Initial gravimetric rate of CO_2 production for various samples normalized per g of catalyst, **(b)** Initial CO_2 STY for various samples normalized per mol of metal. Reaction conditions: temperature 298 K, 0.05 $g_{catalyst}$, 0.83 $cm^3\ s^{-1}$ total flow; total pressure 101 kPa; 4.0 kPa CO, 30.4 kPa O_2, 4.0 kPa N_2 (internal standard), balance He.

To evince the presence of unique active centers in $CoPCF_{16}$@FAU relative to MPC-free FAU, we also tested Na/FAU and metal ion-exchanged FAU (i.e., Co/, Cu/, and Fe/FAU). The initial gravimetric rate of CO_2 production was ~6× higher over $CoPCF_{16}$@FAU than over Co-, Fe-, or Na-containing samples without CoPC. These rates are consistent with a previous study that found Cu-exchanged LTA zeolite to be inactive for CO oxidation, and Co/LTA to be only mildly active, on the basis of the DRUV spectra before and after reaction.[61] Normalizing STYs per mol metal results in even greater disparities in reactivity between CoPC-containing and CoPC-free FAU

samples (Figure 7b). $CoPCF_{16}$@FAU produced CO_2 at a STY of 1.82 mol (mol Co)$^{-1}$ s^{-1}, ~4× higher than $CoPC/CeO_2$ at 498 K,[62] ~6× higher than Co-N-C (273 K), ~40× higher than Co/FAU (this work) and ~180× higher than data reported for Co/MFI (403 K).[63] We note that this site normalization assumes all Co atoms in $CoPCF_{16}$@FAU are equally reactive and accessible, ultimately resulting in the reported initial STYs for this and other samples in Figure 7 representing lower bounds for the CO oxidation STYs. To further test the impact of the zeolite framework, we also tested pure $CoPCF_{16}$ powder, as well as $CoPCF_{16}/C$ and $CoPCF_{16}/SiO_2$ (see Figures S.28 & S.29). The $CoPCF_{16}$ complex with no support produced a small amount of CO_2, ~30× less than $CoPCF_{16}$@FAU. $CoPCF_{16}/SiO_2$ produced CO_2 at a lower rate than $CoPCF_{16}$ powder. $CoPCF_{16}/C$, however, produced CO_2 at a similar initial STY to $CoPCF_{16}$/FAU, which suggests that MPC catalysts benefit from the presence of a support, but whether the presence of a support beneficial depends on the identity of the support.

Cu-containing catalysts were more reactive than those containing Co, Fe, or metal-free samples. $CuPCCl_{16}$@FAU was the most active MPC@FAU sample tested for CO oxidation in this study, but the STY per mol Cu was slightly lower than that measured over $CoPCF_{16}$@FAU, due to the higher metal weight loadings of perchlorinated samples relative to perfluorinated samples. $CuPCCl_{16}$@FAU produced CO_2 at an initial STY of 1.21 mol (mol Cu)$^{-1}$ s^{-1}, ~700× higher than CuO/CeO_2[64] at 428 K.

Zn phthalocyanines also showed similar activity to CoPC-, MnPC-, and CuPC-containing samples. $ZnPCCl_{16}$@FAU produced CO_2 at an initial STY of 0.58 mol (mol Zn)$^{-1}$ s^{-1}, ~160× higher than previous data reported for Zn/MFI at 298 K.[65] $ZnPCF_{16}$@FAU produced CO_2 at an even higher initial STY of 2.0 mol (mol Zn)$^{-1}$ s^{-1}.

Cr Ni, and Mn containing samples were only mildly active at the standard conditions used here. A bar graph of initial STYs for Cr and Ni samples can be found in Figure S.27. $CrPCCl_{16}$@FAU had an initial STY of 0.024 mol (mol Cr)$^{-1}$ s^{-1}. Of all the different MPCs tested in this study, $CrPCCl_{16}$@FAU was the only one that had a lower initial STY than its corresponding MPC/FAU sample. $CrPCCl_{16}$/FAU had an initial STY of 0.326 mol (mol Cr)$^{-1}$ s^{-1}. $NiPCCl_{16}$@FAU was slightly more active, with an initial STY of 0.0392 mol (mol Ni)$^{-1}$ s^{-1}. $MnPCCl_{16}$@FAU produced CO_2 at an initial STY of 0.108 mol (mol Mn)$^{-1}$ s^{-1}, ~55× higher than data reported for amorphous manganese oxide at 423 K.[66] Of all the encapsulated samples tested in this study, only $MnPCCl_{16}$-, $CrPCCl_{16}$-, and $NiPCCl_{16}$@FAU completed less than one turnover before deactivating, while the rest of the encapsulated MPCs completed at least one turnover (see Table S.1). MPC/FAU samples all deactivated before completing one turnover, suggesting either agglomeration of MPCs on the external surface, or that MPC/FAU has a different proclivity for catalytic turnovers in CO oxidation compared to MPC@FAU.

Various pretreatment and co-feed experiments were conducted to probe the origins of catalyst deactivation. Based on results from similar M-N-C catalysts,[19] we were concerned that trace water was entering the system and poisoning the catalyst. $ZnPCCl_{16}$@FAU was pretreated in 3 kPa H_2O (0.83 cm^3 s^{-1} total flow; total pressure 101 kPa) for three hours, but this pretreatment had no effect on the initial CO_2 STY (Figure S.24). Co-feeding the same partial pressure of water during reaction also had no impact on the initial STY (Figure S.24). As discussed in the Section 3.7, the MPCs in this study bind both CO and O_2 strongly, so it is possible that one or both of these reactants was competitively binding to the active sites. As shown in Figure S.25, pretreating $CoPCF_{16}$@FAU in pure oxygen (0.25 cm^3 s^{-1}) for three hours had no impact in the initial STY. However, when the same catalyst was pretreated in dilute CO (0.83 cm^3 s^{-1} total flow; total pressure 101 kPa; 4.0 kPa

CO; balance He) for six hours, the initial CO_2 STY decreased by a factor of ten, from 3.94 to 0.410 mol (mol Co)$^{-1}$ s^{-1}. Without the CO pretreatment, the catalyst completed ~9.5 turnovers, but only 0.7 turnovers after the dilute CO pretreatment (Figure S.30). When the CO partial pressure in the feed was decreased from 4 to 3.5 kPa, the initial CO_2 STY increased to 6.92 mol (mol Co)$^{-1}$ s^{-1}, and the number of cumulative turnovers increased to 16.7 (Figure S.30). This suggests that this reaction is negative order in CO, and the strong adsorption of CO to the metal centers in MPC is a possible cause of deactivation. When these same reactant pretreatment experiments were run over $ZnPCCl_{16}$@FAU (Figure S.26), both pretreatments decreased the initial STY by 10×. While this supports the hypothesis that strong adsorption of reactants to the metal centers in MPC may cause deactivation, which of the two reactants that binds too strongly may be different for each transition metal center in MPC.

These results evince differences in reactivity between metal ions and/or active centers in MPC@FAU and M/FAU samples, which we propose result from the unique local geometry of metal centers in MPC complexes. Further investigation of these effects was performed using computational catalysis approaches.

3.6 Evidence of Encapsulation of MPCs in FAU

Here we summarize the outcomes from experiments described above that suggest the MPCs are occluded within FAU crystallites. First, DRUV spectra of Soxhlet washed MPC@FAU solids still show characteristic Q band indicative of the conjugated π-bond systems in the phthalocyanine complex, while DRUV spectra of Soxhlet washed MPC/FAU solids do not show a Q band (Figure S.9). Second, pre-edge features in XANES data suggest metal centers are in a square planar geometry with a +2-oxidation state as is expected for MPCs (Figure 4). Third, measured micropore volumes of MPC@FAU samples were lower than those measured for

Na/FAU synthesized through the same hydrothermal procedure (Figure 2a). The Soxhlet washing procedure was found to not impact the average micropore volume of washed samples (Figure 2b). Furthermore, when MPC@FAU samples were calcined, the micropore volume increased to that of MPC-free Na/FAU (Figure 2c). Finally, the reactivity in CO oxidation was distinct for materials we termed "MPC@FAU" compared to the comparable MPC/FAU and M/FAU materials. This suggests that the MPC@FAU samples are distinct from those in which MPCs are deposited on the exterior of FAU, and from samples representative of those obtained if the metal central atoms had leached from the MPC during synthesis. Despite these findings, we acknowledge that it is possible there are local defects around the MPCs within these solids that allow for their retention in locations that do not allow their removal via Soxhlet extraction, but that those locations may not be pristine FAU supercages.

3.7 Computational Studies

Binding free energies for CO and O_2 to isolated MPCs (in vacuum, at 298 K) were calculated using the PBE-D3(BJ)//def2-TZVPP/PBE-D3(BJ)/def2-SVP level of theory and are reported in Figure S.42. Of the MPCs tested in this study, only Cr had a significantly greater affinity for dioxygen than CO.

The energetics of candidate CO oxidation reaction mechanisms were obtained by modeling the MPC as a single unit in vacuum without the FAU because modeling MPC in vacuum is a reasonable model choice (Section S.17). Additionally, we considered different catalyst models whereby we explore the role of axial ligands on the energetics of the CO oxidation reaction (Section S.18).

To make connections to experimental results, we considered the obtained experimental results as inputs to computational reaction mechanism discovery. Pretreatment experiments of

$CoPCF_{16}$@FAU with CO or O_2 show that the subsequent reaction rate is insensitive to the O_2 pretreatment while CO pretreatment leads to an order of magnitude reduction in the initial reaction rate. This can be explained by the strong binding of CO compared to O_2 (see Tables S3 to S5) and indicates that CO effectively poisons the catalyst by blocking available active sites. This is in contrast to the positive CO reaction order observed in Whitcomb et al.'s study on a single Co ion in N-doped carbon catalyst (Co-N-C) which suggests that the reaction mechanism for MPCs is distinct from Co-N-C.[19] Therefore, we concluded that the CO oxidation reaction should be initiated by O_2 binding to the metal center in which the reaction can follow an Eley-Rideal (ER) mechanism whereby gas phase CO reacts with bound O_2 or a Langmuir-Hinshelwood (LH) mechanism whereby the CO is co-adsorbed on the MPC before abstracting an O atom from O_2. We highlight that an exhaustive study of the possible CO oxidation reaction mechanisms for all MPCs studied here is beyond the scope of this current work, therefore we focus only on the $CoPCF_{16}$ and $CuPCCl_{16}$ catalysts.

For the $CoPCF_{16}$ and $CuPCCl_{16}$ catalysts, we explored two O_2-initiated and one CO-initiated mechanism. For simplicity, we named the studied mechanisms according to which species adsorbs first on the metal center (O_2 or CO) and the type of step involved in the two CO_2 formation (O abstraction) steps, i.e., either an ER or LH step. Consequently, the three mechanisms we explored are named as follows, O_2-LH-ER mechanism, O_2-ER-ER mechanism, and CO-LH-LH mechanism. For the O_2-LH-ER mechanism (see examples in Figure 8 and Figure S.59), the reaction begins by adsorbing O_2 on the metal center followed by the binding of CO to a nearby pyrrole N to form a bound OOCO complex. The CO can then abstract an O atom from the O_2 (LH step) to form the first CO_2 molecule and leave behind a metal-oxo complex. To form the second CO_2 molecule and close the catalytic cycle, a gas phase CO then abstracts the bound O atom (ER

step). In the O_2-ER-ER mechanism (see examples in Figure S.45 and Figure S.60), the reaction also begins by adsorbing O_2 on the metal center, then both O abstraction step involves a gas phase CO reacting with the bound O_2 or O (both ER steps). Meanwhile, in the CO-LH-LH mechanism (see examples in Figure S.61 and S.61), CO binds first to the metal center followed by the binding of O_2 to the CO to form a bound OOCO complex similar to the work of Whitcomb et al.[19] for single Co ion on nitrogen-doped carbon (Co-N-C). The CO then takes an O atom from the O_2 leaving behind a metal-oxo complex whereby the resulting O atom is inserted between the M-N bond (i.e., M-O-N). We also note that we do not show every possible mechanism based on our nomenclature (for example, O_2-ER-LH) since every other meaningful combination of steps can be derived from the three mechanisms we present here. Based on our calculations, the O_2-LH-ER mechanism gave the lowest barriers for the two O abstraction steps for the $CoPCF_{16}$ and $CuPCCl_{16}$ catalysts, and as such only the O_2-LH-ER mechanism for $CoPCF_{16}$ will be discussed in the following sections in detail while we refer the reader to the Supporting Information (Section S.18) for detailed discussions of the other reaction mechanisms. In addition to the reaction mechanisms, we also hypothesize that the formation of the inert Cu-O-N complex can rationalize the faster deactivation of the $CuPCCl_{16}$ compared to the $CoPCF_{16}$ catalyst (see Section S.18 for additional details).

3.7.1 CO Oxidation via the O_2-LH-ER Reaction Mechanism on $CoPCF_{16}$

Figure 8 shows the calculated potential energy diagram and schematic representation for the O_2-LH-ER mechanism for CO oxidation over the $CoPCF_{16}$ models considered in this work (Figure S.44). For the $CoPCF_{16}$ with no ligand (Figure 8, red pathway, see Figure S.47 for structures), O_2 binds to the Co followed by the formation of the OCOO complex. This is then followed by a transition state that gives an overall barrier of 88 kJ mol^{-1} for the O-O bond breaking to form the

first CO_2 molecule and the Co-oxo complex. The Co-oxo complex then can easily react (free energy barrier of only 30 kJ mol^{-1}) with another CO molecule to form the second CO_2 and close the catalytic cycle.

We also considered MPC models whereby an axial ligand is bound to the MPC which might happen during the synthesis of the FAU and stay intact after the pretreatment of the catalyst (see details in Section S.18). For instance, the MPC might bind to the defective FAU framework. For simplicity, the framework bound MPC was modeled as the MPC axially coordinated to a silicate cluster (see Figure S.44b). Here, (green pathway in Figure 8, see Figure S.48 for structures) the barrier for the formation of the first and second CO_2 molecule is 68, and 21 kJ mol^{-1}, respectively. Next, we further considered a model whereby the MPC is coordinated axially by a hydroxyl ion (Figure S.44c) that originates from NaOH present in the synthesis slurry. Figure 8 (blue pathway) shows the reaction pathway for $CoPCF_{16}$ whereby a hydroxyl ion is axially coordinated to the Co atom (see Figure S.49 for structures). Here, we have an even lower barrier for the formation of the first CO_2 molecule as only 65 kJ mol^{-1} needed to abstract an O atom from the O_2 and produce a CO_2 molecule. Meanwhile, there is only a 22 kJ mol^{-1} barrier required to form the second CO_2 molecule. In addition to this, we also considered CO as a potential ligand due to its strong binding to the metal site (Figure S.44d). Here, (brown pathway in Figure 8, see Figure S.50 for structures) the presence of CO as an axial ligand increases the barrier for the formation of the first CO_2 to an overall barrier of 94 kJ mol^{-1} compared to 88 kJ mol^{-1} for $CoPCF_{16}$ with no axial ligand and supports the hypothesis that CO poisons the catalyst. However, there is no significant change in the barrier for the second CO_2 with a barrier of 29 kJ mol^{-1} compared to 30 kJ mol^{-1} for the $CoPCF_{16}$ with no axial ligand.

From the above mechanistic details, we can see that without any axial ligands the free energy barrier of the first O abstraction is relatively high (88 kJ mol^{-1}), which is too high to explain the catalytic activity observed experimentally at room temperature. However, there is a systematic reduction in the barrier due to the presence of axial ligands except for the CO ligated system where the barrier for the O_2 bond breaking is increased by 6 kJ mol^{-1} to 94 kJ mol^{-1}. We can see that for the silicate ligated system, the O_2 bond breaking barrier (68 kJ mol^{-1}) is reduced by 20 kJ mol^{-1} compared to the $CoPCF_{16}$ with no axial ligand (88 kJ mol^{-1}). In the presence of the hydroxyl ligand,

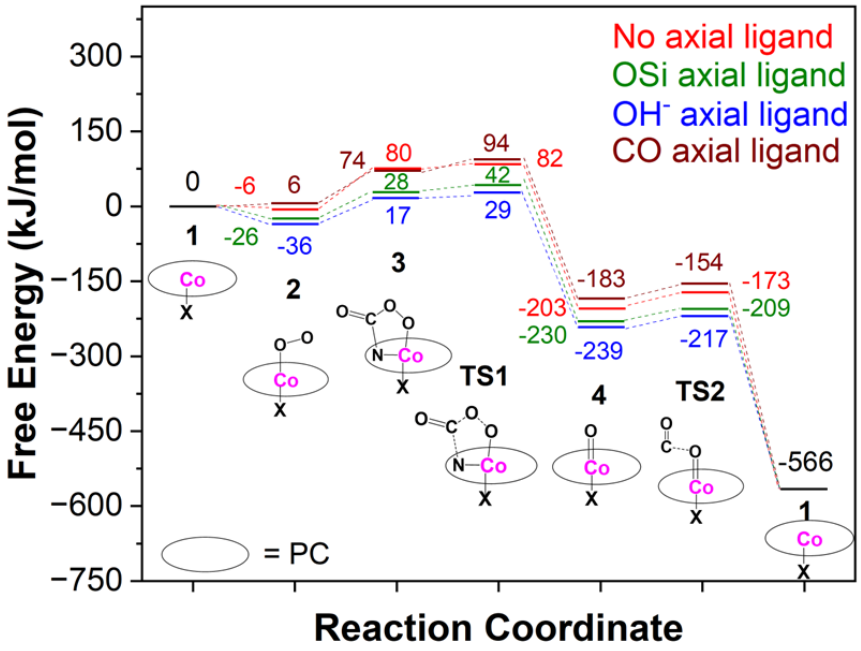

Figure 8. Potential energy diagram for CO oxidation on $CoPCF_{16}$ via the O_2-LH-ER mechanism. Red, brown, green, and blue horizontal and dashed lines indicate energetics with no axial ligand on Co, with CO coordination, silicate coordination, and with hydroxyl ion coordination, respectively. For clarity, the schematic of each state is also shown. X = no ligand, CO, hydroxyl ion, or silicate. See SI for structures corresponding to each state.

the barrier for the O_2 bond breaking is further lowered by 23 kJ mol^{-1} to only 65 kJ mol^{-1} which is more consistent with the experimentally observed reaction rate.

3.7.2 Role of Charge Transfer on CO Oxidation Barrier

To probe the origins of the reduced barrier for the O-O bond breaking step, we generated electron density difference plots for the $CoPCF_{16}$ when O_2 is bound to the Co center with or without axial ligands (Figure 9). These reveal increased electron density on the O atoms in the presence of axial coordination of the hydroxyl ion or the silicate while the electron density on the O atoms in the presence of the CO ligand is comparable to the O atoms in the absence of a ligand (Figure 9). Natural Bond Orbital analysis in Tables S.10 to S.13 also shows increased negative charge on the O atoms as result of the ligands. Specifically, for the silicate ligated case there is an increase in negative charge (-0.11 and -0.16 charge for O_a and O_b, respectively) on the O atoms compared to -0.03 (O_a), and -0.04 (O_b) when there is no ligand. Meanwhile, when the hydroxyl ion is axially bound to the Co center, there is significantly more negative charge on the O atoms (-0.14 and -0.19 compared to -0.03 and -0.04 for $CoPCF_{16}$ without axial ligands, for O_a and O_b, respectively). Lastly, when CO is axially bound to the Co center, there is minimal change in the charge on the O atoms (-0.06 and -0.08 compared to -0.03 and -0.04 for $CoPCF_{16}$ without axial ligands, for O_a and O_b, respectively). As can be seen in the electron density difference plots (Figure 9) below, additional charge from axial ligands is easily transferred via the Co center which help activate the O-O bond and stabilize the transition state. The results suggest that the barrier for the abstraction of the first O atom trends with the amount of charge transferred to the bound O_2 molecule. Therefore, DFT calculations show that an axial ligand can provide additional electron density that can help activate the O-O bond and reduce the barrier for the reaction of CO and the adsorbed O_2 in general.

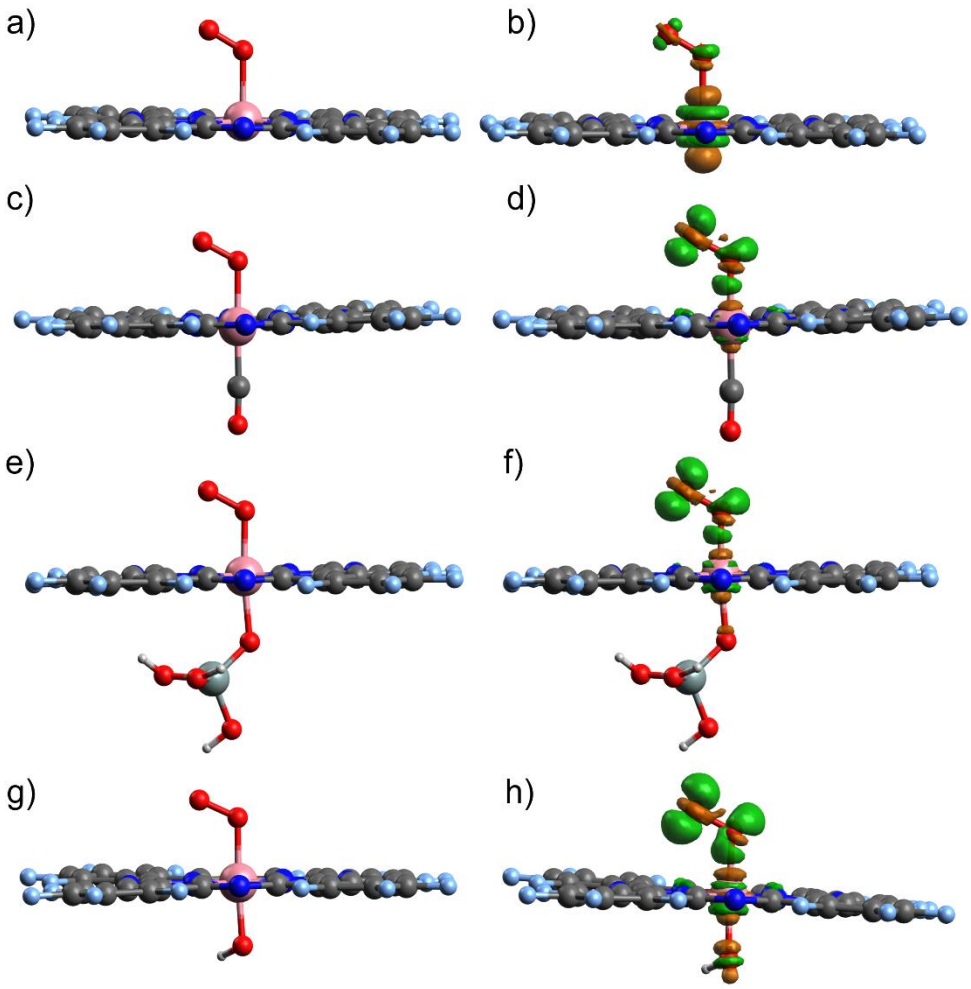

Figure 9. Electron density difference plots showing transfer of electron density to bound O_2 from $CoPCF_{16}$ with a,b) no axial ligand, c,d) CO as ligand, and e,f) silicate as ligand, and g,h) hydroxyl ion ligand. Green and brown regions with isovalue of 0.005 e $Å^{-3}$ indicate electron density accumulation and depletion, respectively. Atom color code: C – gray, H – white, N – blue, O – red, F – cyan, Co – pink, Si – gray.

Conclusions

Reliable synthesis protocols for preparation of MPC@FAU samples were developed, which required use of higher gel Si/Al ratios than previous reports of such materials. These samples were characterized with a broad suite of characterization techniques to demonstrate the phase purity of FAU hosts, encapsulation of MPCs within FAU, and lack of detritus, ion-exchanged metal cations on MPC@FAU samples. These materials can be prepared with a range of metal central atoms from

the 3d transition metals (e.g., Cr, Mn, Fe, Co, Cu, Ni, Zn) using primarily commercially available MPC reagents. Synthetic success largely depends on the solubility of the MPC, which varies greatly with the identity of the peripheral atoms.

MPCs isolated within FAU supercages are useful catalysts for gas-phase chemistries, demonstrated here for aerobic CO oxidation. The metal binding sites in these catalysts are comparable to those in bulk M-N-C catalysts, but with more uniform geometry and coordination of primary binding sites, and the presence of secondary binding pockets (FAU supercages). Metal atoms present in square planar M-N_4 geometry are significantly more reactive than tetrahedral, ion-exchanged metal cations in FAU, with Co-N_4 sites most reactive in CO oxidation at 298 K. Apparent activation energies and reaction orders measured over Co-N-C are consistent with rate-determining O_2 adsorption, based on existing Co-N-C literature. DFT calculations suggest that an axial ligand can provide additional electron density that can help activate the O-O bond and reduce the barrier for the reaction of gas-phase CO and the adsorbed O_2 in general. DFT calculations also showed that the PC can participate by binding CO to the pyrrole N that can help to promote O abstraction from the metal bound O_2. As such, the O_2-activation mechanism is more favorable for MPCs and is a distinct reaction mechanism from N-doped carbons. The synthetic methods reported here, as well as the reactivities in gas-phase oxidations, propound use of MPC@FAU catalysts as functional mimics of widely reported M-N-C, M-zeolite, and M-MOF catalysts. We expect that these will be useful model materials for a broad range of experimental-computational studies in catalysis.

Supporting Information

Supporting Information for this article can be found online. Supporting information includes: catalyst naming scheme; additional computational methods; washing test results; XRD patterns;

process flow diagram; impact of Si:Al ratio on solid yield; table of structural characterization data; additional DRUV-Vis spectra; FTIR spectra; additional XAS spectra; additional kinetic data; regressions used to determine initial rates; N_2 adsorption isotherms; additional EPR spectra; role of He treatment time in CO oxidation; DFT calculated binding free energies; relative stability of encapsulated $ZnPCF_{16}$ geometries; catalyst models for CO oxidation; Natural Bond Order analysis; simulated UV-VIS spectra; simulated XAS spectra.

Declaration of Competing Interests

The authors declare no competing financial interests.

Acknowledgements

The authors acknowledge Dr. Xinyu Li (University of Minnesota) for helpful discussions related to synthesis of FAU, and Prof. Aditya Bhan and Dr. Matt Simons (University of Minnesota) for helpful discussions related to reactor design. We acknowledge Prof. Robert J. Davis (University of Virginia) and Prof. Madelyn Ball (West Virginia University) for helpful discussions related to removal of volatile carbonyls from CO-containing streams. We further acknowledge Prof. Davis and Mr. Colby Whitcomb (University of Virginia) for supplying the CABOT carbon black pearls and their guidance with synthesis of Co-N-C. We acknowledge Prof. Yizhi Xiang and Mr. Genwei Chen from Mississippi State University for assistance collecting ICP-MS data. We acknowledge Simon Bare, Adam Hoffman, and Jiyun Hong (Co-Access team at SSRL) for help with XAS data analysis. We acknowledge Prof. Emeritus Michael K. Bowman for helpful discussions concerning interpretation of the EPR spectra. We also acknowledge Amit Chowdhury for assistance with phthalocyanine synthesis. The authors acknowledge financial support from the National Science Foundation through award number NSF-CBET-2050507. EPI was partially supported by the U.S.

Department of Education as a GAANN Fellow (P200A210069; PI: Yonghyun Kim). A.S and T.S would also like to thank the University of Alabama and the Office of Information Technology for providing high-performance computing resources and support that has contributed to these research results. This work was also made possible in part by a grant of high-performance computing resources and technical support from the Alabama Supercomputer Authority. This research also used resources of the National Energy Research Scientific Computing Center (NERSC), a U.S. Department of Energy Office of Science User Facility located at Lawrence Berkeley National Laboratory, operated under Contract No. DE-AC02-05CH11231 using NERSC award BES-ERCAP m4299 for 2023.

References

1. Parton, R. F.; Vankelecom, I. F. J.; Casselman, M. J. A.; Bezoukhanova, C. P.; Uytterhoeven, J. B.; Jacobs, P. A., An efficient mimic of cytochrome P-450 from a zeolite-encaged iron complex in a polymer membrane. *Nature* **1994,** *370*, 541-544.
2. Simons, M. C.; Vitillo, J. G.; Babucci, M.; Hoffman, A. S.; Boubnov, A.; Beauvais, M. L.; Chen, Z.; Cramer, C. J.; Chapman, K. W.; Bare, S. R.; Gates, B. C.; Lu, C. C.; Gagliardi, L.; Bhan, A., Structure, Dynamics, and Reactivity for Light Alkane Oxidation of Fe(II) Sites Situated in the Nodes of a Metal–Organic Framework. *Journal of the American Chemical Society* **2019,** *141*, 18142-18151.
3. Kester, P. M.; Miller, J. T.; Gounder, R., Ammonia Titration Methods To Quantify Brønsted Acid Sites in Zeolites Substituted with Aluminum and Boron Heteroatoms. *Industrial & Engineering Chemistry Research* **2018,** *57*, 6673-6683.
4. Harris, J. W.; Cordon, M. J.; Di Iorio, J. R.; Vega-Vila, J. C.; Ribeiro, F. H.; Gounder, R., Titration and quantification of open and closed Lewis acid sites in Sn-Beta zeolites that catalyze glucose isomerization. *Journal of Catalysis* **2016,** *335*, 141-154.
5. Nikashina, V. A.; Zvereva, L. I.; Olshanova, K. M.; Potapova, M. A., Study of the selectivity of different types of zeolites towards some non-ferrous metals. *Journal of Chromatography A* **1976,** *120*, 155-158.
6. Ostroski, I. C.; Barros, M. A. S. D.; Silva, E. A.; Dantas, J. H.; Arroyo, P. A.; Lima, O. C. M., A comparative study for the ion exchange of Fe(III) and Zn(II) on zeolite NaY. *Journal of Hazardous Materials* **2009,** *161*, 1404-1412.
7. Vermoortele, F.; Ameloot, R.; Alaerts, L.; Matthessen, R.; Carlier, B.; Fernandez, E. V. R.; Gascon, J.; Kapteijn, F.; De Vos, D. E., Tuning the catalytic performance of metal–organic frameworks in fine chemistry by active site engineering. *Journal of Materials Chemistry* **2012,** *22*, 10313-10321.
8. Chen, M. J.; Rathke, J. W., Phthalocyanines in Hydrocarbon Activation. *ChemInform* **1997,** *28*.

9. Sehlotho, N.; Nyokong, T., Catalytic activity of iron and cobalt phthalocyanine complexes towards the oxidation of cyclohexene using tert-butylhydroperoxide and chloroperoxybenzoic acid. *Journal of Molecular Catalysis A: Chemical* **2004,** *209*, 51-57.
10. Sorokin, A.; Meunier, B.; Séris, J.-L., Efficient oxidative dechlorination and aromatic ring cleavage of chlorinated phenols catalyzed by iron sulfophthalocyanine. *Science* **1995,** *268*, 1163-1166.
11. Basu, B.; Satapathy, S.; Bhatnagar, A. K., Merox and related metal phthalocyanine catalyzed oxidation processes. *Catalysis Reviews—Science and Engineering* **1993,** *35*, 571-609.
12. de Vos, D. E.; Sels, B. F.; Jacobs, P. A., Immobilization of homogeneous oxidation catalysts. *Advances in Catalysis* **2001,** *46*, 1-87.
13. Schulz-Ekloff, G.; Wöhrle, D.; Iliev, V.; Ignatzek, E.; Andreev, A., Study of the Structure and the Redox Reactivity of Nax Encapsulated Co(Ii)-Phthalocyanine. *Studies in Surface Science and Catalysis* **1989,** *46*, 315-325.
14. Onodera, T.; Suzuki, S.; Mizukami, T.; Kanzaki, H., Enhancement of oxygen reduction activity with addition of carbon support for non-precious metal nitrogen doped carbon catalyst. *Journal of Power Sources* **2011,** *196*, 7994-7999.
15. Lefèvre, M.; Proietti, E.; Jaouen, F.; Dodelet, J.-P., Iron-Based Catalysts with Improved Oxygen Reduction Activity in Polymer Electrolyte Fuel Cells. *Science* **2009,** *324*, 71-74.
16. Akula, S.; Mooste, M.; Zulevi, B.; McKinney, S.; Kikas, A.; Piirsoo, H.-M.; Rähn, M.; Tamm, A.; Kisand, V.; Serov, A.; Creel, E. B.; Cullen, D. A.; Neyerlin, K. C.; Wang, H.; Odgaard, M.; Reshetenko, T.; Tammeveski, K., Mesoporous textured Fe-N-C electrocatalysts as highly efficient cathodes for proton exchange membrane fuel cells. *Journal of Power Sources* **2022,** *520*, 230819.
17. Wang, Q.; Yang, Y.; Sun, F.; Chen, G.; Wang, J.; Peng, L.; Chen, W.-T.; Shang, L.; Zhao, J.; Sun-Waterhouse, D.; Zhang, T.; Waterhouse, G. I. N., Molten NaCl-Assisted Synthesis of Porous Fe-N-C Electrocatalysts with a High Density of Catalytically Accessible FeN4 Active Sites and Outstanding Oxygen Reduction Reaction Performance. *Advanced Energy Materials* **2021,** *11*, 2100219.
18. Xie, J.; Kammert, J. D.; Kaylor, N.; Zheng, J. W.; Choi, E.; Pham, H. N.; Sang, X.; Stavitski, E.; Attenkofer, K.; Unocic, R. R.; Datye, A. K.; Davis, R. J., Atomically Dispersed Co and Cu on N-Doped Carbon for Reactions Involving C–H Activation. *ACS Catalysis* **2018,** *8*, 3875-3884.
19. Whitcomb, C. A.; Sviripa, A.; Schapowal, M. I.; Mamedov, K.; Unocic, R. R.; Paolucci, C.; Davis, R. J., Mechanistic Insights on the Low-Temperature Oxidation of CO Catalyzed by Isolated Co Ions in N-Doped Carbon. *ACS Catalysis* **2022,** *12*, 15529-15540.
20. Herron, N.; Stucky, G. D.; Tolman, C. A., Shape selectivity in hydrocarbon oxidations using zeolite encapsulated iron phthalocyanine catalysts. *Journal of the Chemical Society, Chemical Communications* **1986**, 1521.
21. Bols, M. L.; Rhoda, H. M.; Snyder, B. E. R.; Solomon, E. I.; Pierloot, K.; Schoonheydt, R. A.; Sels, B. F., Advances in the synthesis, characterisation, and mechanistic understanding of active sites in Fe-zeolites for redox catalysts. *Dalton Transactions* **2020,** *49*, 14749-14757.
22. Di Iorio, J. R.; Nimlos, C. T.; Gounder, R., Introducing Catalytic Diversity into Single-Site Chabazite Zeolites of Fixed Composition via Synthetic Control of Active Site Proximity. *ACS Catalysis* **2017,** *7*, 6663-6674.

23. Otto, T.; Zones, S. I.; Iglesia, E., Challenges and strategies in the encapsulation and stabilization of monodisperse Au clusters within zeolites. *Journal of Catalysis* **2016,** *339*, 195-208.
24. Raja, R.; Ratnasamy, P., Oxyhalogenation of Aromatics over Copper Phthalocyanines Encapsulated in Zeolites. *Journal of Catalysis* **1997,** *170*, 244-253.
25. Sirotin, S. V.; Tolbin, A. Y.; Moskovskaya, I. F.; Abramchuk, S. S.; Tomilova, L. G.; Romanovsky, B. V., Heterogenized Fe(III) phthalocyanine: Synthesis, characterization and application in liquid-phase oxidation of phenol. *Journal of Molecular Catalysis A: Chemical* **2010,** *319*, 39-45.
26. Gabrielov, A. G.; Balkus, K. J.; Bell, S. L.; Bedioui, F.; Devynck, J., Faujasite-type zeolites modified with iron perfluorophthalocyanines: Synthesis and characterization. *Microporous Materials* **1994,** *2*, 119-126.
27. Steinbach, F.; Joswig, H.-J., Metal phthalocyanines used as catalysts in gas phase reactions: X. Decomposition and reduction of NO catalyzed by crystalline monomeric β-metal phthalocyanines of the first transition period. *Journal of Catalysis* **1978,** *55*, 272-280.
28. Bedioui, F., Zeolite-encapsulated and clay-intercalated metal porphyrin, phthalocyanine and Schiff-base complexes as models for biomimetic oxidation catalysts: an overview. *Coordination Chemistry Reviews* **1995,** *144*, 39-68.
29. Romanovsky, B. V.; Gabrielov, A. G., Zeolite-included phthalocyanines: Synthesis, characterization and catalysis in ox-red reactions. *Journal of Molecular Catalysis* **1992,** *74*, 293-303.
30. Balkus, K. J.; Welch, A. A.; Gnade, B. E., The encapsulation of Rh(III) phthalocyanines in zeolites X and Y. *J Incl Phenom Macrocycl Chem* **1991,** *10*, 141-151.
31. Awala, H.; Gilson, J.-P.; Retoux, R.; Boullay, P.; Goupil, J.-M.; Valtchev, V.; Mintova, S., Template-free nanosized faujasite-type zeolites. *Nature Materials* **2015,** *14*, 447-451.
32. Dong, A.; Shakouri, A.; Karakalos, S.; Blom, D.; Williams, C. T.; Regalbuto, J. R., The preparation of silica supported, dilute limit PdAu alloys via simultaneous strong electrostatic adsorption. *Catalysis Science & Technology* **2023,** *13*, 3020-3034.
33. Borghard, W. S.; Sheppard, E. W.; Schoennagel, H. J., An automated, high precision unit for low-pressure physisorption. *Review of Scientific Instruments* **1991,** *62*, 2801-2809.
34. Law, D. P.; Blakeney, A. B.; Tkachuk, R., The Kubelka–Munk equation: some practical considerations. *Journal of Near Infrared Spectroscopy* **1996,** *4*, 189-193.
35. Kubelka, P.; Munk, F., An article on optics of paint layers. *Z. Tech. Phys* **1931,** *12*, 259-274.
36. Stoll, S.; Schweiger, A., EasySpin, a comprehensive software package for spectral simulation and analysis in EPR. *Journal of Magnetic Resonance* **2006,** *178*, 42-55.
37. Spicher, S.; Grimme, S., Robust Atomistic Modeling of Materials, Organometallic, and Biochemical Systems. *Angewandte Chemie International Edition* **2020,** *59*, 15665-15673.
38. Hickmott, P. W., Enamines: recent advances in synthetic, spectroscopic, mechanistic, and stereochemical aspects-I. *Tetrahedron* **1982,** *38*, 1975-2050.
39. Perdew, J. P.; Burke, K.; Ernzerhof, M., Generalized Gradient Approximation Made Simple. *Physical Review Letters* **1996,** *77*, 3865-3868.
40. Weigend, F.; Ahlrichs, R., Balanced basis sets of split valence, triple zeta valence and quadruple zeta valence quality for H to Rn: Design and assessment of accuracy. *physical chemistry chemical physics* **2005,** *7*, 3297-3305.
41. Grimme, S.; Ehrlich, S.; Goerigk, L., Effect of the damping function in dispersion corrected density functional theory. *Journal of Computational Chemistry* **2011,** *32*, 1456-1465.

42. Chai, J.-D.; Head-Gordon, M., Systematic optimization of long-range corrected hybrid density functionals. *The Journal of Chemical Physics* **2008,** *128*, 084106.
43. Banau, O. R., Y.; Joly, Y., The FDMNES code. *International Tables for Crystallography* **2021**.
44. Bunău, O.; Joly, Y., Self-consistent aspects of x-ray absorption calculations. *Journal of Physics: Condensed Matter* **2009,** *21*, 345501.
45. Sharma, P.; Yeo, J.-g.; Han, M. H.; Cho, C. H., Knobby surfaced, mesoporous, single-phase GIS-NaP1 zeolite microsphere synthesis and characterization for H 2 gas adsorption. *Journal of Materials Chemistry A* **2013,** *1*, 2602-2612.
46. Maldonado, M.; Oleksiak, M. D.; Chinta, S.; Rimer, J. D., Controlling Crystal Polymorphism in Organic-Free Synthesis of Na-Zeolites. *Journal of the American Chemical Society* **2013,** *135*, 2641-2652.
47. Ziminov, A. V.; Ramsh, S. M.; Terukov, E. I.; Trapeznikova, I. N.; Shamanin, V. V.; Yurre, T. A., Correlation dependences in infrared spectra of metal phthalocyanines. *Semiconductors* **2006,** *40*, 1131-1136.
48. Giovannetti, R., The use of spectrophotometry UV-Vis for the study of porphyrins. *Macro to nano spectroscopy* **2012**, 87-108.
49. Yahiro, H.; Kimoto, K.; Yamaura, H.; Komaguchi, K.; Lund, A., Copper–phthalocyanine encapsulated into zeolite-Y with high Si/Al: An EPR study. *Chemical physics letters* **2005,** *415*, 126-130.
50. Yahiro, H.; Naka, T.; Kuramoto, T.; Kurohagi, K.; Okada, G.; Shiotani, M., An EPR study on oxygen molecule adduct of Co (II)-phthalocyanines encapsulated into zeolites. *Microporous and mesoporous materials* **2005,** *79*, 291-297.
51. Blakemore, J. D.; Hull, J. F.; Crabtree, R. H.; Brudvig, G. W., Aqueous speciation and electrochemical properties of a water-soluble manganese phthalocyanine complex. *Dalton Transactions* **2012,** *41*, 7681-7688.
52. Assour, J. M.; Goldmacher, J.; Harrison, S. E., Electron spin resonance of vanadyl phthalocyanine. *The Journal of Chemical Physics* **1965,** *43*, 159-165.
53. Assour, J. M., Solvent effects on the spin resonance spectra of cobalt phthalocyanine. *Journal of the American Chemical Society* **1965,** *87*, 4701-4706.
54. Bletsa, E.; Solakidou, M.; Louloudi, M.; Deligiannakis, Y., Oxidative catalytic evolution of redox- and spin-states of a Fe-phthalocyanine studied by EPR. *Chemical Physics Letters* **2016,** *649*, 48-52.
55. Gaur, A.; Shrivastava, B. D.; Joshi, S. K. In *Copper K-edge XANES of Cu (I) and Cu (II) oxide mixtures*, 2009; IOP Publishing: p 012084.
56. Gorelik, T. E.; Habermehl, S.; Shubin, A. A.; Gruene, T.; Yoshida, K.; Oleynikov, P.; Kaiser, U.; Schmidt, M. U., Crystal structure of copper perchlorophthalocyanine analysed by 3D electron diffraction. *Acta Crystallographica Section B Structural Science, Crystal Engineering and Materials* **2021,** *77*, 662-675.
57. Ha, S. Y.; Park, J.; Ohta, T.; Kwag, G.; Kima, S., In Situ Iron K-Edge XANES Study of Iron Phthalocyanine Irreversibly Adsorbed on an Electrode Surface. *Electrochemical and solid-state letters* **1999,** *2*, 461.
58. Semyannikov, P. P.; Basova, T. V.; Grankin, V. M.; Igumenov, I. K., Vapour pressure of some phthalocyanines. *Journal of Porphyrins and Phthalocyanines* **2000,** *4*, 271-277.

59. Jiang, H.; Ye, J.; Hu, P.; Wei, F.; Du, K.; Wang, N.; Ba, T.; Feng, S.; Kloc, C., Fluorination of Metal Phthalocyanines: Single-Crystal Growth, Efficient N-Channel Organic Field-Effect Transistors and Structure-Property Relationships. *Scientific Reports* **2014,** *4*, 7573.
60. Xu, J.; White, T.; Li, P.; He, C.; Yu, J.; Yuan, W.; Han, Y.-F., Biphasic Pd−Au Alloy Catalyst for Low-Temperature CO Oxidation. *Journal of the American Chemical Society* **2010,** *132*, 10398-10406.
61. Förster, H.; Witten, U., Spectroscopic investigations on sorption and oxidation of carbon monoxide in transition metal ion-exchange zeolites A: Studies on cobalt, nickel and copper forms. *Zeolites* **1987,** *7*, 517-521.
62. Song, Y.; Hu, S.; Cai, D.; Xiao, J.; Zhou, S.-F.; Zhan, G., Cobalt Phthalocyanine Supported on Mesoporous CeO2 as an Active Molecular Catalyst for CO Oxidation. *ACS Applied Materials & Interfaces* **2022,** *14*, 9151-9160.
63. Ivanin, I. A.; Krotova, I. N.; Udalova, O. V.; Zanaveskin, K. L.; Shilina, M. I., Synergistic Catalytic Effect of Cobalt and Cerium in the Preferential Oxidation of Carbon Monoxide on Modified Co/Ce/ZSM-5 Zeolites. *Kinetics and Catalysis* **2021,** *62*, 798-811.
64. Papavasiliou, J.; Rawski, M.; Vakros, J.; Avgouropoulos, G., A Novel Post-Synthesis Modification of CuO-CeO₂

Catalysts: Effect on Their Activity for Selective CO Oxidation. *ChemCatChem* **2018,** *10*, 2096-2106.
65. Qi, G.; Xu, J.; Su, J.; Chen, J.; Wang, X.; Deng, F., Low-Temperature Reactivity of Zn+ Ions Confined in ZSM-5 Zeolite toward Carbon Monoxide Oxidation: Insight from in Situ DRIFT and ESR Spectroscopy. *Journal of the American Chemical Society* **2013,** *135*, 6762-6765.
66. Tian, F.-X.; Zhu, M.; Liu, X.; Tu, W.; Han, Y.-F., Dynamic structure of highly disordered manganese oxide catalysts for low-temperature CO oxidation. *Journal of Catalysis* **2021,** *401*, 115-128.